

N69-20880  
TMX-52581

**NASA TECHNICAL  
MEMORANDUM**

NASA TM X-52581

NASA TM X-52581

**WIND TUNNEL INSTALLATION EFFECTS ON ISOLATED  
AFTERBODIES AT MACH NUMBERS FROM 0.56 TO 1.5**

by Bernard J. Blaha and Donald L. Bresnahan  
Lewis Research Center  
Cleveland, Ohio  
1969

This information is being published in preliminary form in order to expedite its early release.

WIND TUNNEL INSTALLATION EFFECTS ON ISOLATED  
AFTERBODIES AT MACH NUMBERS FROM 0.56 TO 1.5

by Bernard J. Blaha and Donald L. Bresnahan

Lewis Research Center  
Cleveland, Ohio

NATIONAL AERONAUTICS AND SPACE ADMINISTRATION



# WIND TUNNEL INSTALLATION EFFECTS ON ISOLATED AFTERBODIES AT MACH NUMBERS FROM 0.56 TO 1.5

By Bernard J. Blaha and Donald L. Bresnahan

Lewis Research Center  
National Aeronautics and Space Administration  
Cleveland, Ohio

## ABSTRACT

Pressure distributions and boundary-layer data were obtained on three different diameter models used for afterbody studies in the Lewis Research Center 8- by 6-Foot Supersonic Wind Tunnel to determine the quality of the local flow approaching the afterbody region. The support methods for these models included sting mounts and various types of support struts appropriate for jet-exit models. Data were obtained at zero degrees angle-of-attack and Mach numbers from 0.56 to 1.5. Afterbody pressure drag data and the effects of boundary-layer momentum thickness on afterbody pressure drag were also obtained on several models for 15-degree conical boattails with jet-boundary simulators.

## SUMMARY

Pressure distribution and boundary-layer data were obtained on three different diameter models used for afterbody studies in the Lewis Research Center 8- by 6-Foot Supersonic Wind Tunnel to determine the quality of the local flow approaching the afterbody region. The support methods for these models included sting mounts and various types of support struts appropriate for jet-exit models. Data were obtained at zero degrees angle-of-attack and Mach numbers from 0.56 to 1.5. Afterbody pressure drag data and the effects of boundary-layer momentum thickness on afterbody pressure drag were also obtained on 15-degree conical boattails with jet-boundary simulators.

Installation effects were generally minor at subsonic speeds for all models tested. The largest installation effects occurred at Mach numbers between 1.1 and 1.5 and were the greatest for the strut-supported models. The single-swept strut provided the least disturbance of all of the strut systems tested and should be considered for cold-flow jet-exit models. The strut-supported model currently being used at the Lewis Research Center provided boattail pressure drags that were relatively free from installation effects outside the low supersonic speed range. In general, increasing

boundary-layer momentum thickness resulted in reduced boattail pressure-drag coefficient, particularly at high subsonic speeds.

### INTRODUCTION

The Lewis Research Center is conducting wind tunnel programs to study the performance of exhaust nozzles for airbreathing propulsion systems (ref. 1-4). As part of this effort, pressure-drag characteristics of various afterbody shapes have been investigated on isolated nacelles, both with and without a jet (ref. 5 and 6), under a simulated wing (ref. 7), and on nacelles mounted at the trailing edge of a delta wing using a model of the F-106B aircraft (ref. 8). During the course of these studies, it was observed that pressure drag of geometrically-similar boattails was influenced by tunnel installation techniques and by geometric features of the model forebodies. In most wind tunnel tests of exhaust nozzles, it is particularly difficult to obtain interference-free data since jet models usually preclude the use of a support sting and require a supporting strut ahead of the nozzle. These struts can be relatively large since they must support the model and house instrumentation and air lines. Details of the design of support struts become important since they are a source of disturbance to the local flow field approaching the nozzle. Thus, comparison of boattail drag and nozzle performance from different wind tunnel programs and facilities becomes difficult.

To illustrate the problems of support interference on jet exit measurements, this report presents pressure distributions measured in the 8- by 6-Foot Supersonic Wind Tunnel for three different diameter models. The support methods for these models included sting mounts and various types of support struts appropriate for jet-exit models. These distributions indicate deviations in the quality of the local flow approaching the nozzle which vary with support method. Data are presented at zero degrees angle-of-attack at Mach numbers from 0.56 to 1.5. In addition, boundary-layer data and its effect on the afterbody pressure drag of 15-degree conical boattails with jet-boundary simulators are also presented. Finally, the boattail pressure drags measured on the jet-exit model currently in use at the Lewis Research Center are compared to those obtained with a small diameter sting-mounted model.

### SYMBOLS

A	area
c	chord
$C_D$	drag coefficient - $\text{drag}/q_0 A_{\text{max}}$

d	diameter
l	length
M	Mach number
p	static pressure
q	dynamic pressure
r	radius
t	thickness
v	velocity
x	measurement parallel to model axis
y	radial distance from model surface
$\delta$	boundary-layer thickness
$\theta$	boundary-layer momentum thickness
$\Delta$	increment

#### Subscripts

max	maximum
$\beta$	boattail
0	free-stream

### APPARATUS AND PROCEDURE

A summary of all model configurations is shown in table I. Four basic models were evaluated for this test: (1) a sting-supported 19.16 cm diameter model; (2) a sting-supported 20.32 cm diameter model with two swept dummy struts; (3) a sting-supported 20.32 cm diameter model with and without a single-swept dummy strut; and (4) a 21.59 cm diameter single straight strut-supported model. The latter model was designed for testing with and without a cold-air jet and is the model currently being used at the Lewis Research Center to measure the thrust minus drag characteristics of various nozzle concepts (e.g., ref. 1-4).

Figure 1 shows the tunnel installation and instrumentation details of the 10.16 cm model. It had a 10-degree half-angle conical forebody, and stings having diameters of 0.405 and 0.670  $d_{max}$  were used for model support. The sting with diameter equal to the model base diameter of 0.670  $d_{max}$  was used with the boattail afterbody to simulate the jet boundary that would exist with an exit-to-local-static-pressure ratio of 1.00. Figures 1(a), 1(b), and 1(c) show schematic diagrams of the 10.16 cm model with cylindrical sections 11.53  $d_{max}$ , 6.55  $d_{max}$ , and 4.72  $d_{max}$  in length. Geometric and instrumentation details of the cylindrical afterbody and conical afterbodies are shown in figures 1(d), 1(e), and 1(f). The cylindrical afterbody was used to evaluate the static pressure environment of the afterbody region as influenced by terminal shock waves, wall-reflected expansion and compression waves from the forebody, and wall-generated disturbances. Two 15-degree conical boattails were investigated; one had a sharp edge at the nacelle juncture, fig. 1(e), and the other had a 0.50  $d_{max}$  radius of curvature, fig. 1(f). Both boattails had a ratio of base diameter to maximum diameter of 0.67. The instrumentation of the rearward-facing portion of the afterbodies was area weighted in order to facilitate the calculation of boattail pressure drag. The method of instrumentation and calculation is described in detail in reference 6. The instrumentation along the cylindrical portion of the model is shown in figures 1(g) and 1(h). Figure 1(i) shows details of the boundary-layer rake which was used to survey the local flow field ahead of the afterbody region and to measure boundary-layer thickness and momentum thickness. The boundary-layer survey plane was located 0.25  $d_{max}$  ahead of the model-afterbody interface. The model was tested in a test section with 3.1 percent porosity walls, and model blockage was 0.18 percent.

Figure 2 shows the tunnel installation and instrumentation details for one of the 20.32 cm models. This model was sting supported but used two dummy struts mounted to the tunnel side walls. These struts were representative of those required for support of a cold-air jet-exit model of the type described in reference 9. The model forebody was a 10-degree half-angle conical tip followed by a 24.74  $d_{max}$  circular arc; overall  $l/d_{max}$  of the nose section was 5.0. The dummy struts were swept back at 45 degrees with a thickness-to-chord ratio of 0.09. The leading-wedge total angle was 15 degrees, and the trailing-wedge angle was 22°54'. Figure 2(a) shows a plan view of the model with cylindrical section length of 11.64  $d_{max}$ . Figure 2(b) shows the cylindrical afterbody that was used to evaluate the static pressure environment of the afterbody region. Figure 2(c) shows the static pressure instrumentation on the cylindrical portion of the model. The test section wall porosity was 5.8 percent for this installation and model blockage was 0.73 percent, exclusive of support struts, and 2.58 percent with struts.



Figure 3(a) shows the tunnel installation of the second 20.32 cm model. This model was a sting-supported cone cylinder with a 15-degree half-angle conical forebody. Figure 3(b) shows the instrumentation details of the model. Static pressure orifices were located along the cylindrical portion of the model at 90° and 180° from the vertical centerline. Pressure orifices located at the strut attachment region were not used when the strut was installed. The model was tested with and without a single-swept, floor-mounted dummy strut which also was representative of that required for support of a cold-air jet-exit model. The strut was swept at 30 degrees and the thickness-to-chord ratio was 0.0673. Leading and trailing-wedge angles were 15 degrees. The model was tested with a test section wall porosity of 5.8 percent. Model blockage was 0.73 percent without the strut and 1.86 percent with the strut.

The tunnel installation and instrumentation details of the 21.59 cm model are shown in figure 4. Use of this model configuration in jet-exit tests is reported in references 1 to 4. The model forebody was a tangent ogive with an  $l/d_{max}$  of 3.0. The model was supported by a single straight strut with a thickness-to-chord ratio of 0.035. Leading and trailing-wedge angles were 10 degrees. The model cylindrical section length was 13.15  $d_{max}$ . Although a support sting was not used, the boattailed afterbody was tested with a simulated jet with a diameter of 0.670  $d_{max}$ . Figures 4(b) and 4(c) show the afterbody geometries evaluated with this model. The boattailed afterbody was geometrically similar to that tested on the 10.16 cm model, and was instrumented in the same manner. Figure 4(d) shows the static pressure instrumentation along the cylindrical portion of the model at 0, 90, and 180 degrees from the vertical centerline. Details of the boundary-layer rakes are shown in figure 4(e). Three rakes were used to survey the boundary layer just ahead of the end of the model. The model was tested in a test section with walls of 5.8 percent porosity. Model blockage was 0.82 percent, exclusive of the support strut, and 1.93 percent with the strut.

Pressure distributions on all the models were ratioed to a computed value of free-stream static pressure,  $p_0$ , upstream of the model nose. In prior calibrations of this tunnel (ref. 10 and 11) a relationship was determined between the operational variables (compressor speed, flexible nozzle position, second throat position, and plenum chamber suction pressure) such that the flow was most uniform over the length of the test section and so that model pressure distributions most nearly matched those of flight vehicles. For each of these tunnel settings, the free-stream Mach number was determined from the ratio of an average tunnel wall static pressure (near the beginning of the perforated region) to free-stream total pressure. At Mach numbers below 1.5 it was determined that this total pressure was equal to the average tunnel bellmouth total pressure. In subsequent testing of research models, the free-stream

Mach number is controlled by this prior calibration of the tunnel operational variables. The free-stream static pressure is computed from the measured bellmouth total pressure and the isentropic relationship with free-stream Mach number. Although a measured wall static pressure could also be used, it is sensitive to flow disturbances from the nose of the research model, whereas the measured bellmouth pressure is not. Therefore, the computed value is regarded as being more reliable.

## RESULTS AND DISCUSSION

The pressure distributions on the four models with cylindrical afterbodies are shown in figures 5, 6, 7, and 8. Data are shown over the length of the model from the cone-shoulder juncture for the sting-mounted 10.16 cm model and aft of the struts for the 20.32 cm and 21.59 cm models. These distributions are used to note the magnitude and location of disturbances on the models by comparing local pressures to free-stream static pressure. The afterbody locations are indicated on the sketches at the top of each figure to facilitate a comparison of disturbances in the region of the afterbody over the range of Mach numbers tested.

The pressure distributions along the 10.16 cm sting-mounted model are shown in figure 5 at several Mach numbers. There were no major disturbances at the subsonic speeds as indicated by the flat pressure distributions in the vicinity of the afterbodies. In general, the pressure downstream of the shoulder recovered to 0.99 of free-stream static pressure. A decrease in pressure can be seen near the aft edge of the model; however, as indicated in reference 10, this is a normal decrease resulting from flow expansion around the model base. At Mach 1.0 the terminal shock appears near the location of the afterbody on the shortest ( $4.72 d_{\max}$ ) model. Identification of the disturbances on the figures at Mach numbers greater than 1.0 were obtained from calibration data for a similar 10.16 cm model reported in reference 10. Results at Mach 1.0 and Mach 1.1 indicate that the terminal shock would be located near the afterbody of the intermediate ( $6.55 d_{\max}$ ) model at Mach 1.05. At Mach 1.1, the terminal shock is positioned near the afterbody location of the long ( $11.53 d_{\max}$ ) model. A tunnel wall disturbance was observed at the afterbody location of the  $4.72 d_{\max}$  and  $6.55 d_{\max}$  models at Mach 1.2, and the  $11.53 d_{\max}$  model at Mach 1.26. No major pressure disturbances were noted at Mach 1.37 or 1.47. In general, the magnitude of the disturbances are not large on this model and varied from 3 to 5 percent of free-stream static pressure

at Mach numbers greater than 1.0. The peak disturbance occurred at Mach 1.2. Boattail drag coefficients obtained between Mach numbers of 1.0 and 1.3 could be influenced by tunnel disturbances to some extent but those at other Mach numbers are not. Because of these results, drag measured with this model for boattailed afterbodies with jet-boundary simulators was considered to be comparatively free of extraneous installation effects.

The pressure distributions along the 20.32 cm sting-mounted model with and without double-swept struts are shown in figure 6. The reference station for  $x = 0$  is about 0.65 model diameters downstream of the trailing edge of the strut. Due to its length, the aft portion of the model extended into a region of the test section which, as described in references 10 and 11, is influenced by a subsonic flow acceleration. This flow acceleration results in a decrease in aft-end tunnel pressure and a corresponding pressure gradient on models located near the end of the test section. As described in reference 11, control of this aft-end flow acceleration has been gained by varying the tunnel second throat in conjunction with the plenum chamber suction. By varying these parameters at a given Mach number, a series of tunnel settings were determined (and are presented in ref. 11) that resulted in more uniform pressure distributions on a series of calibration models that extended into the aft region of the test section. These same tunnel settings were then used with the 20.32 cm model. As indicated by the flat pressure distributions in figure 6, these tunnel settings resulted in favorable pressure distribution at the subsonic speeds. No major pressure disturbances were noted for Mach numbers up to 1.05, and the pressures upstream of the afterbody were between 0.99 of free-stream static and free-stream static. Since strut effects on pressure distribution were small at these low speeds, results are only shown with struts. It must be noted, however, that these results do not reflect the possible effect that the model struts might have on the boundary layer, which was not measured on this model. Large disturbances were observed at Mach numbers from 1.10 through 1.27, particularly with the struts. These disturbances were as much as 20 percent of free-stream static pressure and appear to be the greatest at Mach numbers 1.1 and 1.2. It is probable that all afterbody drag data obtained above Mach 1.05 are influenced by tunnel and model disturbances to some extent. Without the struts, the magnitudes of disturbances were less and their location was displaced. At higher Mach numbers, the disturbance effects were diminished and the addition of struts did not produce a major effect.

Figure 7 shows the static pressure distribution on the 20.32 cm model with and without a single 30-degree swept strut at the supersonic Mach numbers. Downstream of the strut location, the presence of the strut had a relatively small effect on the pressure distributions. The magnitudes of the pressure disturbances were substantially less than the double struts of figure 6.

The pressure distributions along the 21.59 cm single straight strut-mounted model are shown in figure 8. Due to the length of this model, the technique for setting tunnel conditions described in reference 11 was again used at subsonic speeds. As seen in figure 8, these tunnel settings resulted in favorable pressure distributions aft of the strut at the subsonic speeds. The maximum deviation in the region upstream of the afterbody juncture is observed at Mach 0.9 where the pressure level is approximately 0.98 of free-stream static. No major pressure disturbances were noted in the region of the afterbody at speeds up to Mach 1.0. At the higher speeds, results for the 20.32 cm diameter sting-mounted model are again repeated for reference purposes to indicate strut effects. With the strut, large disturbances were present at Mach numbers from 1.10 to 1.46 with magnitudes of 8 to 19 percent of free-stream static pressure. The disturbances with the greatest magnitudes were observed at Mach numbers 1.20 and 1.26. It is probable that all afterbody drag data obtained at Mach numbers from 1.10 to 1.46 are influenced by model and tunnel disturbances. The general magnitude of the disturbances in the supersonic region was about the same for the 20.32 cm double-strut model and the 21.59 cm single straight-strut model, although the location of the disturbances was different for the two models.

The magnitude of disturbances measured on each of the models over the range of Mach numbers investigated is summarized in figure 9. For the sting-supported models, only the pressures on the last eight model diameters of length were considered, and for the strut-supported models, the last three model diameters. The two sting-supported models generally had minor disturbances throughout the Mach number range. Both the single-straight strut and the double-swept strut showed large disturbances at Mach numbers from 1.1 to 1.5. The single-swept strut appears to be the most attractive of the three strut configurations for supporting cold-air jet-exit models. The maximum disturbance for this model was less than 10 percent of free-stream static pressure. This was not much greater than that obtained with the sting-supported models, which had maximum disturbances of 6 percent of free-stream static pressure.

The afterbody boundary-layer characteristics for the 10.16 cm model are shown in figure 10 and are relatively insensitive to Mach number. The boundary-layer thickness was taken as that point where the local velocity was 99 percent of the maximum velocity at the end of the rake. Typical boundary-layer profiles for the three model lengths are shown in figure 11. These profiles are compared with a  $1/7$  power profile as shown by the solid line and indicate a fully-developed turbulent boundary layer. The 21.59 cm model boundary-layer characteristics are shown in figure 12 and are also

insensitive to Mach number. At all Mach numbers, the boundary layer at 0 degrees was noticeably affected by the wake of the model-support strut. This result indicates that the strut does influence the flow over the afterbody even though the effects are not reflected in the local static pressure distributions. A typical boundary-layer profile on the 21.59 cm model is shown in figure 13 for the rake at  $180^\circ$  and Mach number 0.9. This profile is also compared with a  $1/7$  power profile and also indicates a fully-developed turbulent boundary layer.

In figure 14 is shown the ratio of boundary-layer momentum thickness to  $d_{max}$  for the 10.16 cm model and the 21.59 cm model for the rake at 180 degrees. The momentum thickness was determined based on the local conditions at the outermost probe of the rake assuming constant total temperature and constant static pressure through the boundary layer. In figure 15 the effect of boundary-layer momentum thickness on boattail pressure drag is summarized for the 10.16 cm model. Data are presented for boattails with radius ratios of 0 and 0.5 and jet-boundary simulators at Mach numbers from 0.6 to 1.0. Data are also presented without the jet-boundary simulators but with a sting having a diameter of  $0.405 d_{max}$ . The differences in boattail drag for the different sting sizes and radius ratios were expected and are well documented, for example in reference 6. In general, for configurations with the same sting size relative to model diameter and same radius ratio, increasing the ratio of boundary-layer momentum thickness to model diameter reduces the boattail pressure drag coefficient. This effect was generally larger for the thinner values of momentum thickness and decreased for thicker values of momentum thickness. The largest effects were observed for Mach numbers between 0.8 and 0.95.

A comparison between boattail pressure drag measured on the 21.59 cm model and the longest 10.16 cm model is presented for a range of Mach numbers in figure 16 for a 15-degree conical boattail and jet-boundary simulators. As mentioned previously, the 21.59 cm model is currently being used at the Lewis Research Center to evaluate the thrust-minus-drag characteristics of various nozzle concepts for airbreathing propulsion systems. The sting-supported 10.16 cm model provided the installation with the least disturbances over the Mach number range investigated. It is felt that the boattail pressure drag measured with this model would be relatively free of both model and tunnel installation effects. Its drag is, therefore, presented and used as a basis for assessing the installation effects on the larger strut-supported jet-exit model. It should be noted that the measured momentum thickness approaching the boattail on the 21.59 cm model is greater than that measured on the long 10.16 cm model. However, the results presented in figure 15 indicate that both of

these configurations are in a region ( $\theta/d_{\max}$  from 0.012 to 0.022) where the effects of momentum thickness are relatively minor.

The results presented in figure 16 indicate that the boattail pressure drag measured on the larger strut-supported jet-exit model agree favorably with those measured on the smaller sting-supported model. Both models indicate a sharp reduction in boattail pressure drag at a Mach number of 1.1 as the terminal shock passes over the boattail. It is concluded, therefore, that the jet-exit model provides external drag that is relatively free from installation effects, particularly at subsonic speeds.

### SUMMARY OF RESULTS

Pressure distributions on three different diameter models used for afterbody studies in the 8- by 6-Foot Supersonic Wind Tunnel were obtained to determine the quality of the local flow approaching the nozzle. The support methods for these models included sting mounts and various types of support struts appropriate for jet-exit models. Boundary-layer data and the boundary-layer effect on afterbody pressure drag for  $15^\circ$  boattails with jet-boundary simulators were also obtained. Also boattail drag measurements were compared for several models. The following observations were made:

1. At subsonic Mach numbers, static pressures measured on all models tested were generally within 1 to 2 percent of free-stream static pressure. The peak static pressure disturbances were obtained at Mach numbers from 1.1 to 1.5. These disturbances were within 6 percent of free-stream static pressure for the sting-supported models and as large as 20 percent for the strut-supported models.
2. Based on measured static-pressure distributions, the single-swept strut provided the least disturbances of the three-strut systems evaluated. It would warrant serious consideration as a support system for cold-flow jet-exit models.
3. The strut-supported jet-exit model in use at the Lewis Research Center provides boattail pressure drags that are relatively free from installation effects outside the low supersonic speed range.
4. In general, increasing boundary-layer momentum thickness resulted in reduced boattail pressure-drag coefficients.

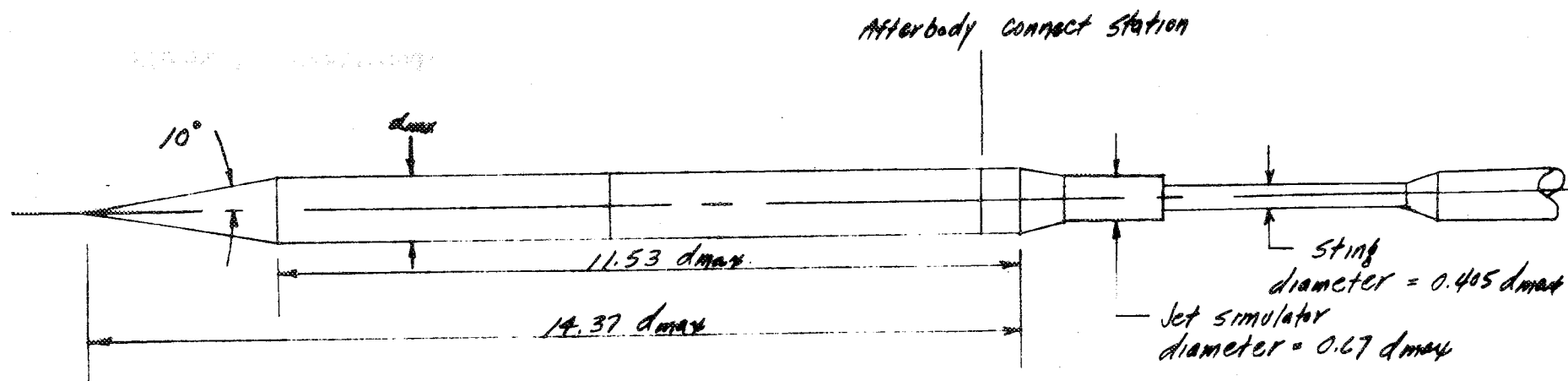
REFERENCES

1. Bresnahan, Donald L.; and Johns, Albert L.: Cold Flow Investigation of a Low-Angle Turbojet Plug Nozzle With Fixed Throat and Translating Shroud at Mach Numbers From 0 to 2.0. NASA TM X-1619, 1968.
2. Steffen, Fred W.; and Jones, John R.: Performance of a Wind Tunnel Model of an Aerodynamically-Positioned Variable Flap Ejector at Mach Numbers From 0 to 2.0. NASA TM X-1639, 1968.
3. Wasko, Robert A.; and Harrington, Douglas E.: Performance of a Collapsible Plug Nozzle Having Either Two-Position Cylindrical or Variable Angle Floating Shrouds at Mach Numbers From 0 to 2.0. NASA TM X-1657, 1968.
4. Bresnahan, Donald L.: Experimental Investigation of a  $10^\circ$  Conical Turbojet Plug Nozzle With Iris Primary and Translating Shroud at Mach Numbers From 0 to 2.0. NASA TM X-1709, 1968.
5. Harrington, Douglas E.: Jet Effects on Boattail Pressure Drag of Isolated Ejector Nozzles at Mach Numbers From 0.60 to 1.47. NASA TM X-1785, 1969.
6. Shrewsbury, George D.: Effect of Boattail Junction Shape on Pressure Drag Coefficients of Isolated Afterbodies. NASA TM X-1517, 1968.
7. Shrewsbury, George D.: Effect of a Simulated Wing on the Pressure-Drag Coefficients of Various  $15^\circ$  Boattails at Mach Numbers From 0.56 to 1.00. NASA TM X-1662, 1968.
8. Blaha, Bernard J.; and Mikkelsen, Daniel C.: Wind Tunnel Investigation of Airframe Installation Effects on Underwing Engine Nacelles at Mach Numbers From 0.56 to 1.46. NASA TM X-1683, 1968.
9. Beheim, Milton A.: Off-Design Performance of Divergent Ejectors. NACA RM E58G10a, 1958.
10. Mitchell, Glenn A.: Blockage Effects of Cone-Cylinder Bodies on Perforated Wind Tunnel Wall Interference. NASA TM X-1655, 1968.
11. Mitchell, Glenn A.: Effect of Model Forebody Shape on Perforated Tunnel Wall Interference. NASA TM X-1656, 1968.

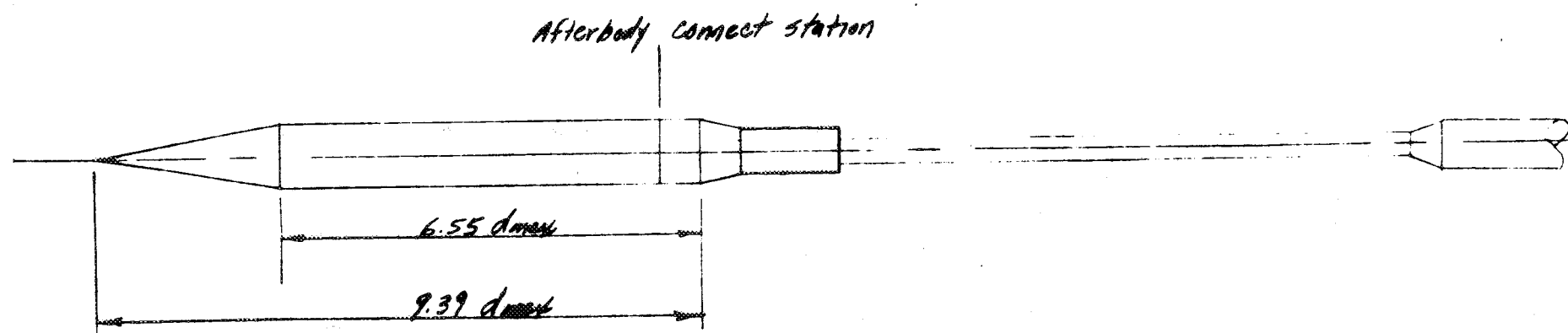
TABLE I CONFIGURATION SUMMARY

MODEL DIAMETER	NOSE SHAPE	STRUT	MODEL $l/d_{max.}$	AFTERBODY
10.16 cm ↓	20° CONE ↓	NONE ↓	11.53 ↓ 6.55 ↓ 4.72 ↓	CYLINDRICAL 15° SHARP 15° RADIUS CYLINDRICAL 15° SHARP 15° RADIUS CYLINDRICAL 15° SHARP 15° RADIUS
20.32 cm ↓	CIRCULAR-ARC 30° CONE ↓	DOUBLE SWEPT SINGLE SWEPT NONE	11.64 13.26 13.26	CYLINDRICAL CYLINDRICAL CYLINDRICAL
21.59 cm ↓	(TANGENTFOGIVE $l/d = 3.0$ )	(SINGLE STRAIGHT)	13.15 ↓	CYLINDRICAL 15° SHARP



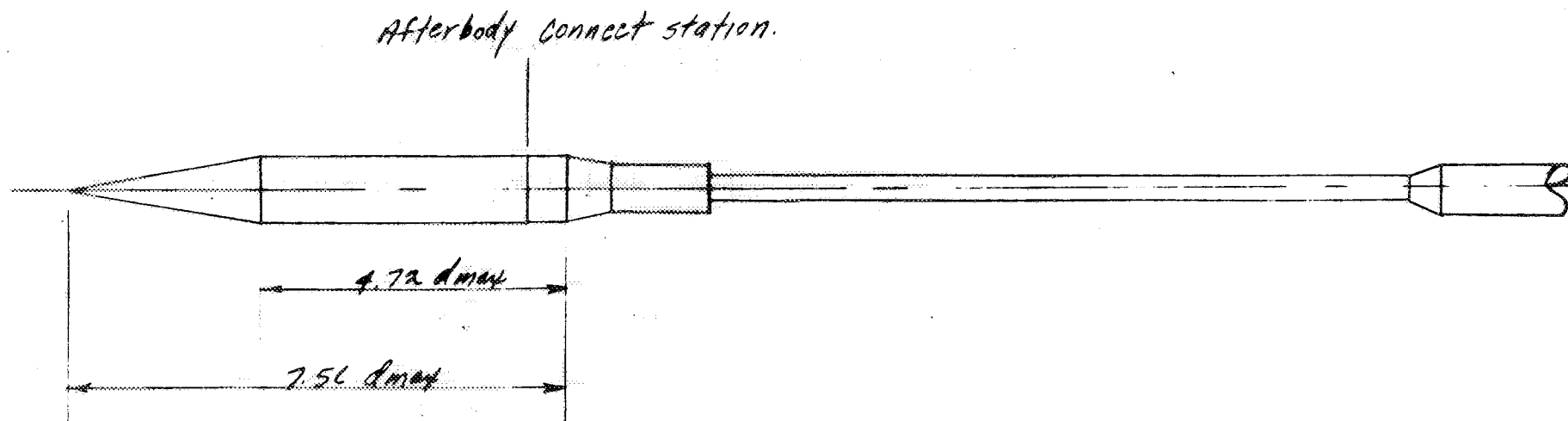


(a) Long model. Model length, 11.53  $d_{max}$ .

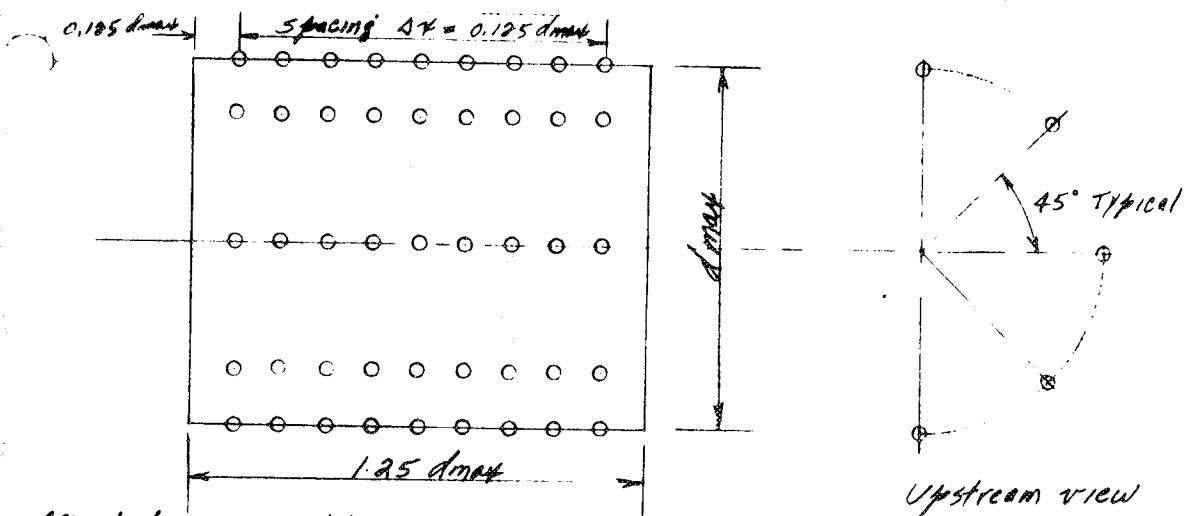


(b) Intermediate model. Model length, 6.55  $d_{max}$ .

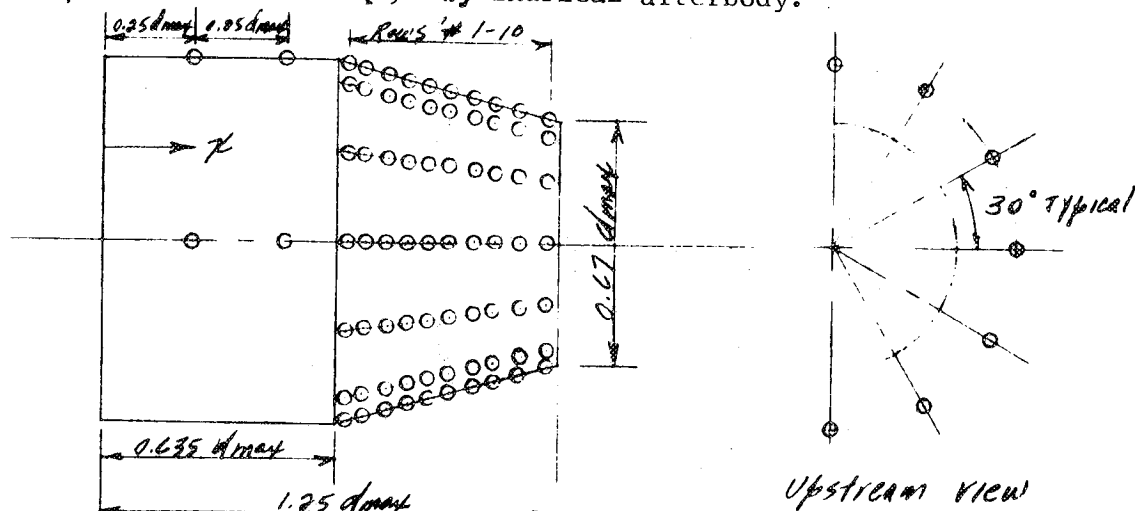
Figure 1. Installation and instrumentation details of 10-16 cm ( $d_{max}$ .) model.



(c) Short model. Model length,  $4.72 d_{max}$ .

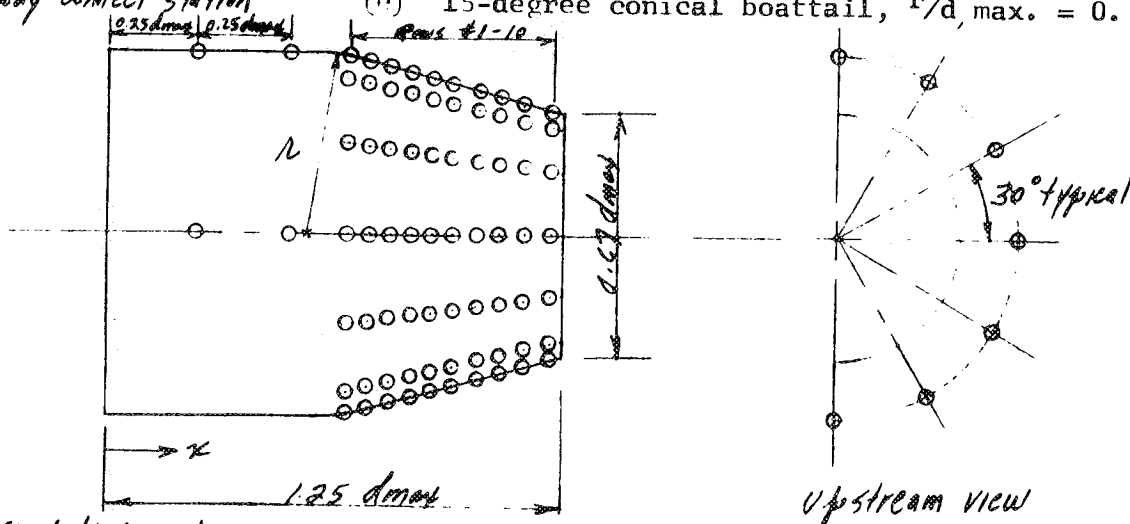


Afterbody connect station (d) Cylindrical afterbody.



Row #	$r/d_{max}$
1	0.668
2	0.715
3	0.773
4	0.830
5	0.885
6	0.945
7	1.010
8	1.070
9	1.140
10	1.213

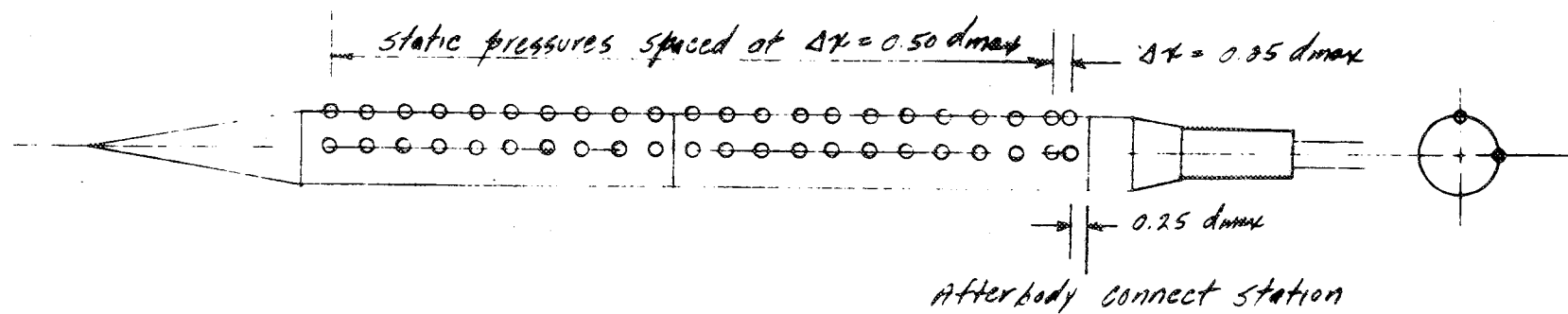
Afterbody connect station (e) 15-degree conical boattail,  $r/d_{max} = 0$ .



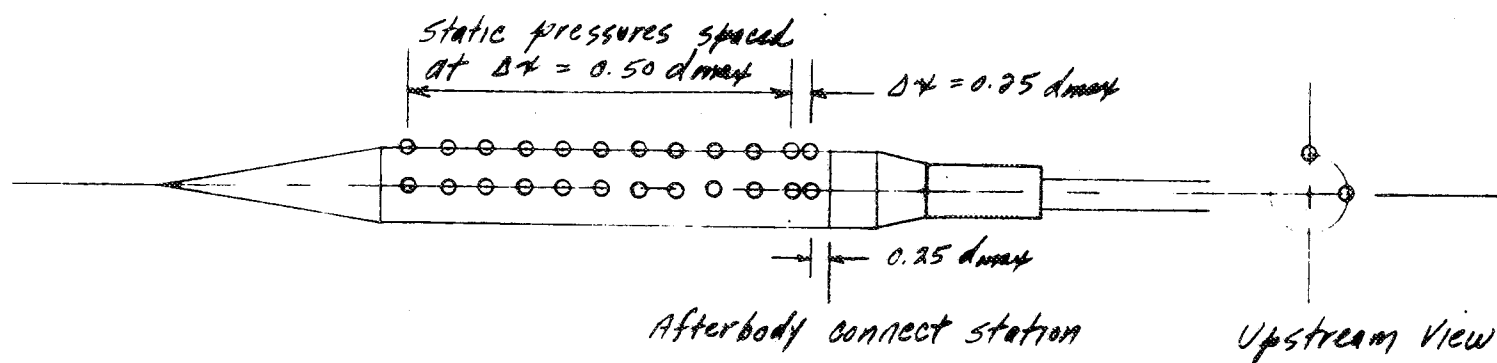
Row #	$r/d_{max}$
1	0.668
2	0.715
3	0.773
4	0.830
5	0.885
6	0.945
7	1.010
8	1.070
9	1.140
10	1.213

Afterbody connect station

(f) 15-degree conical boattail,  $r/d_{max} = 0.50$ .



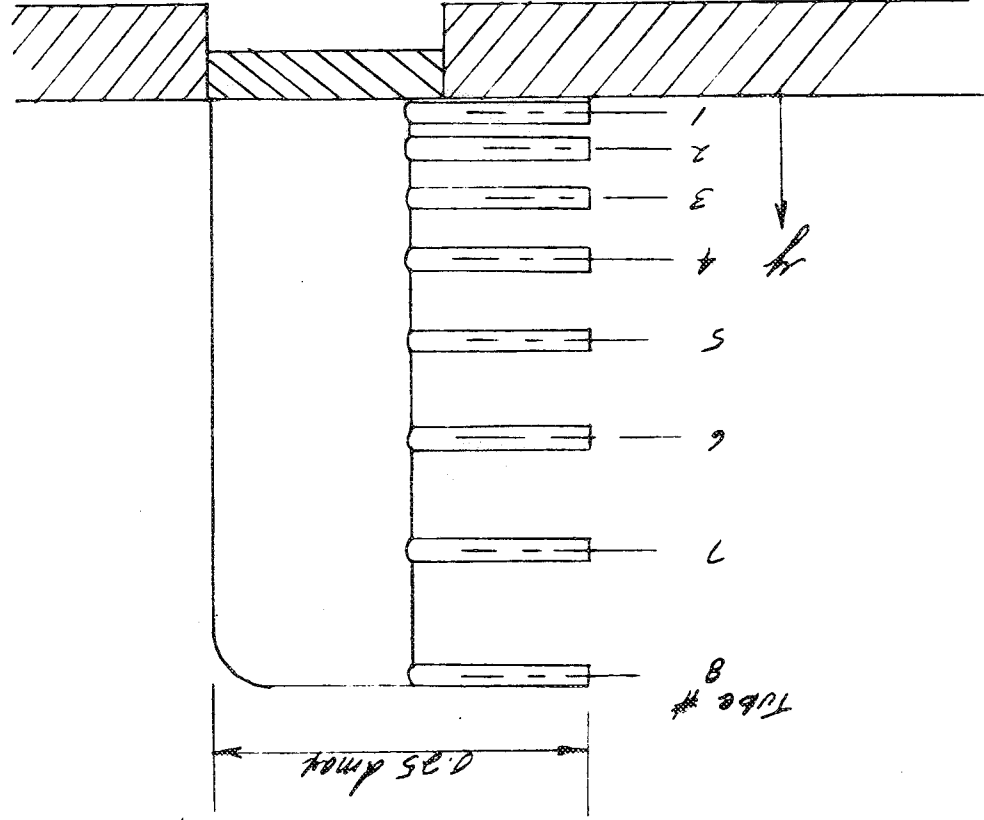
(g) Body static pressures on long model.



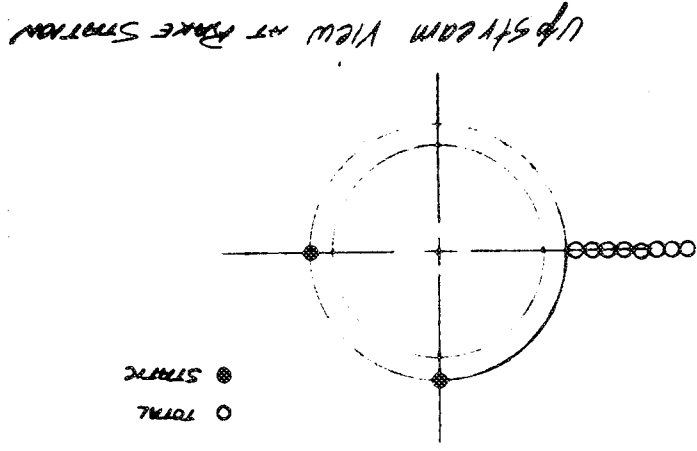
(h) Body static pressures on intermediate model.

Figure 1. Concluded.

(1) Boundary-layer survey rake.



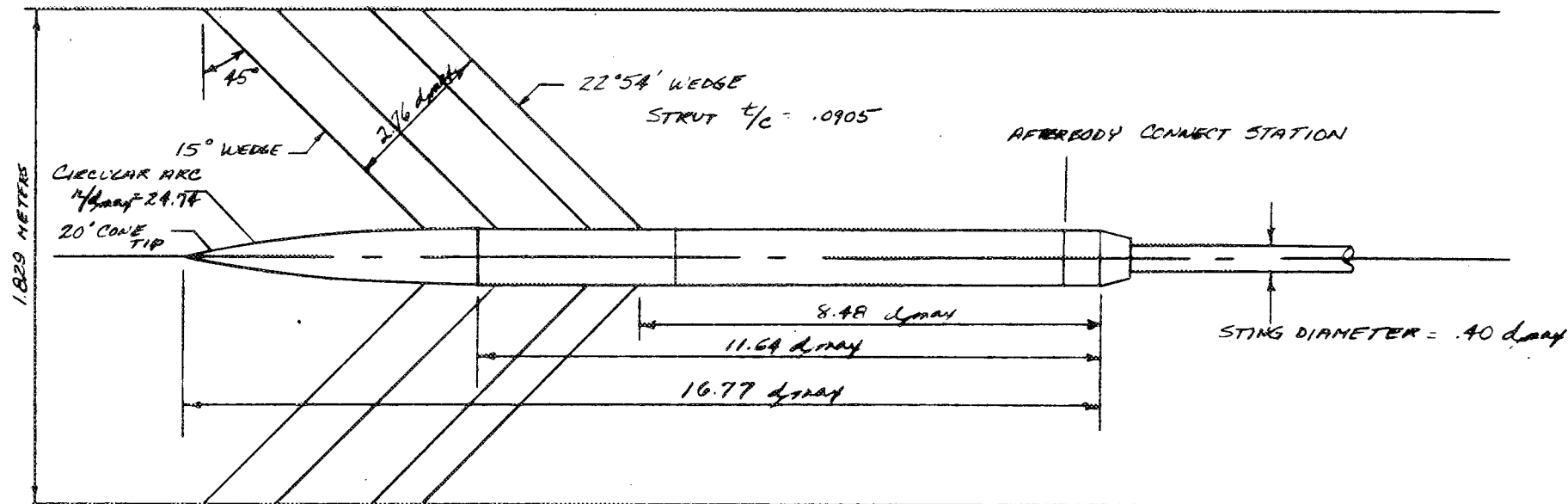
Afterbody connect station



Tube #	$\frac{1}{2}$ diam
1	0.375
2	.293
3	.220
4	.158
5	.105
6	.063
7	.032
8	.011

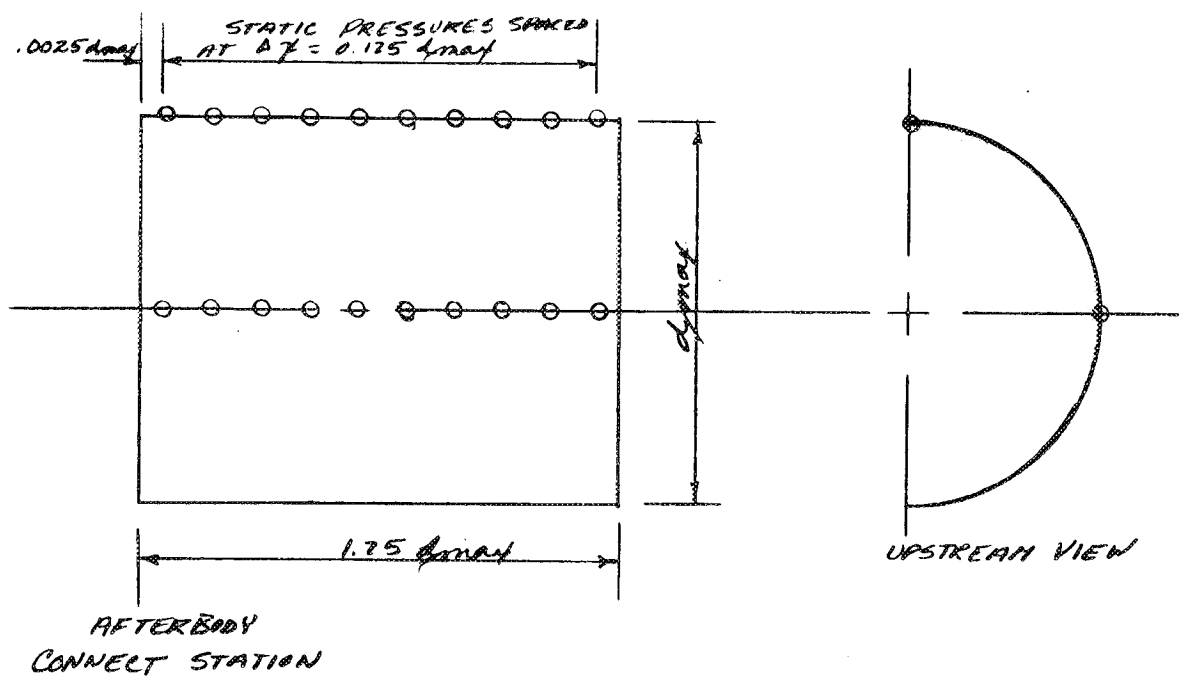
● STATIC  
○ TOTAL

Upstream view of rake station



(a) Installation in 8- by 6-Foot Supersonic Wind Tunnel.

Figure 2. Installation and instrumentation details of 20.32 cm ( $d_{max}$ ) double swept strut model.



(b) Cylindrical afterbody.

Figure 2. Continued.

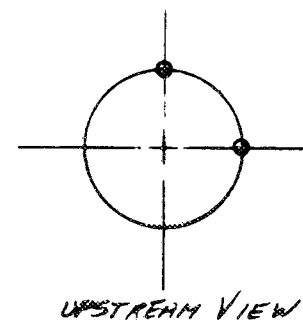
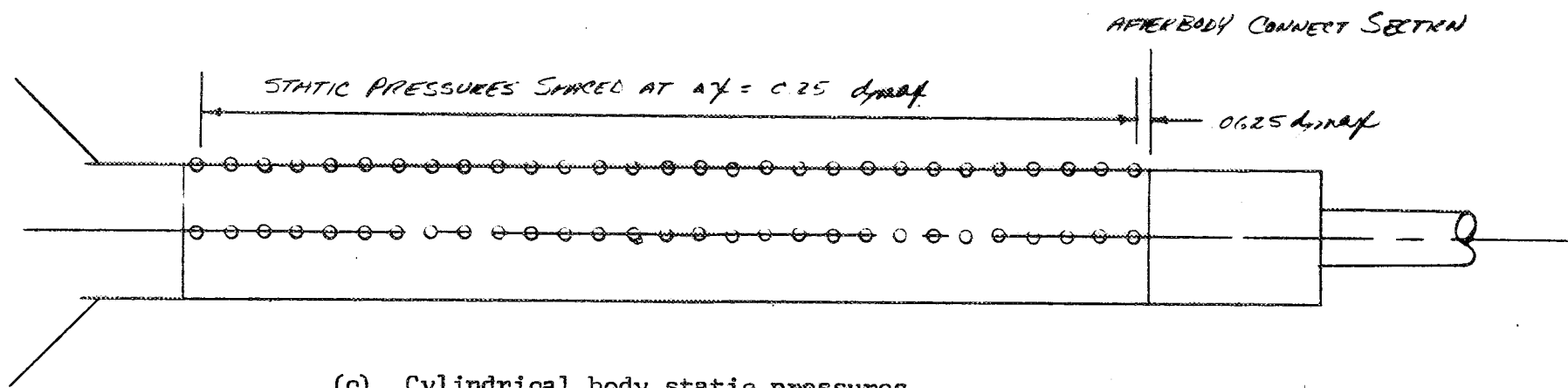
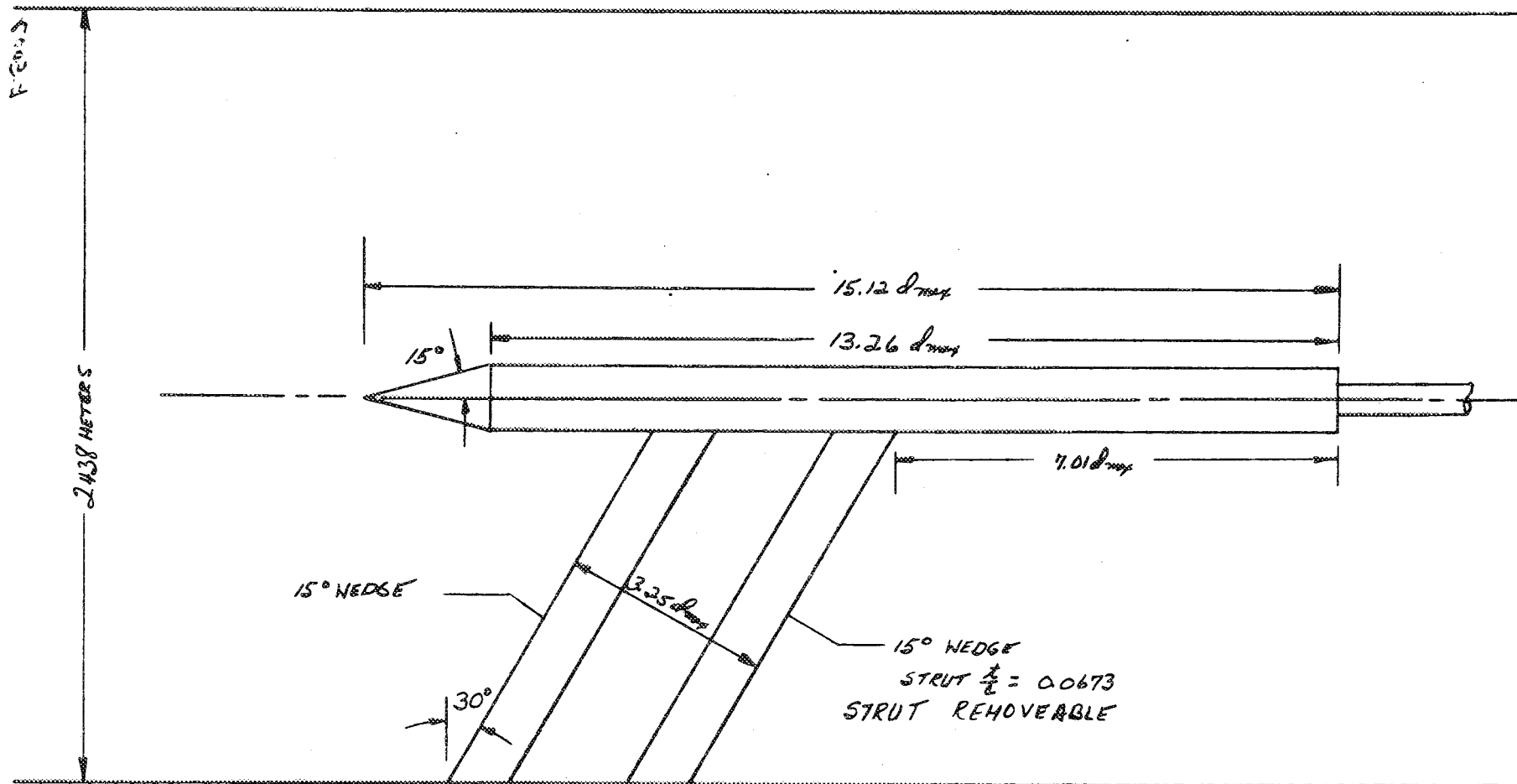


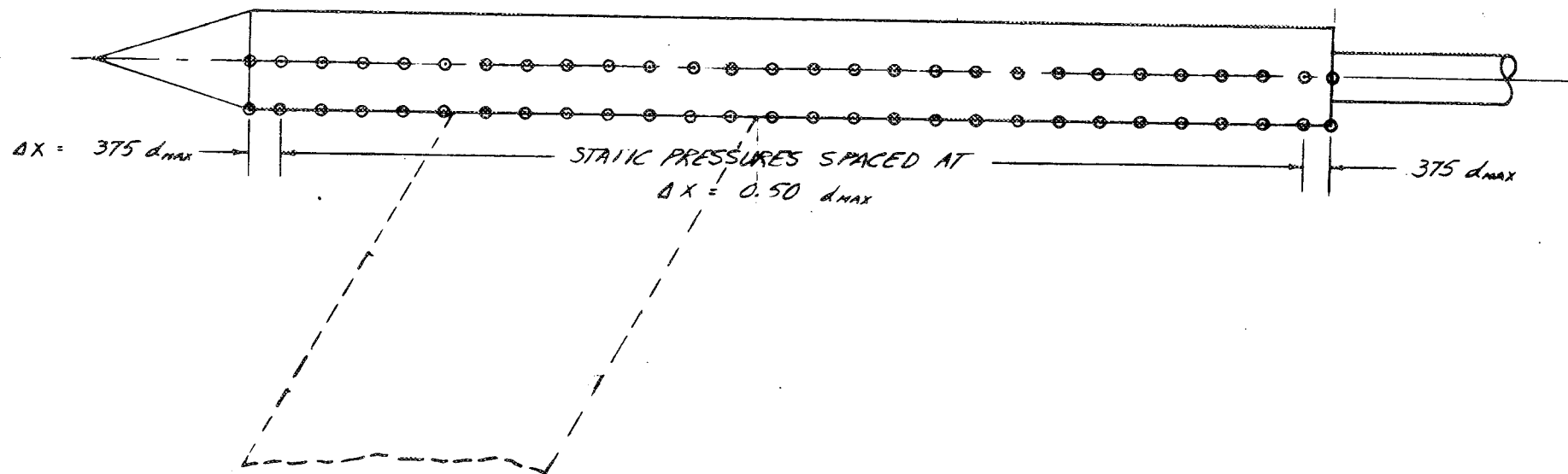
Figure 2. Concluded.





(a) Installation in 8- by 6-Foot Supersonic Wind Tunnel.

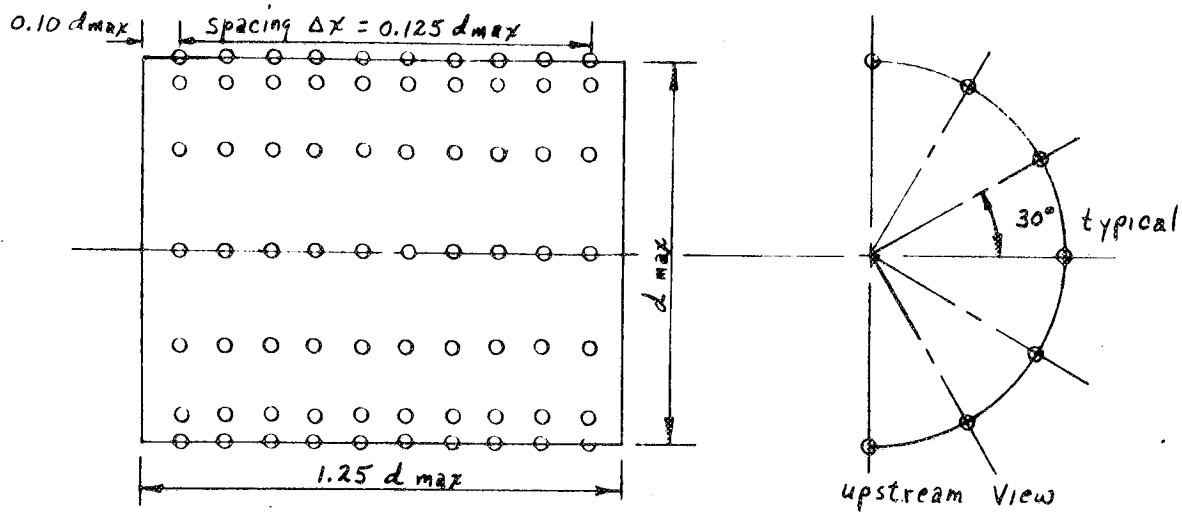
Figure.3. Installation and instrumentation details of the 20.32 cm ( $d_{max}$ ) single swept strut model.



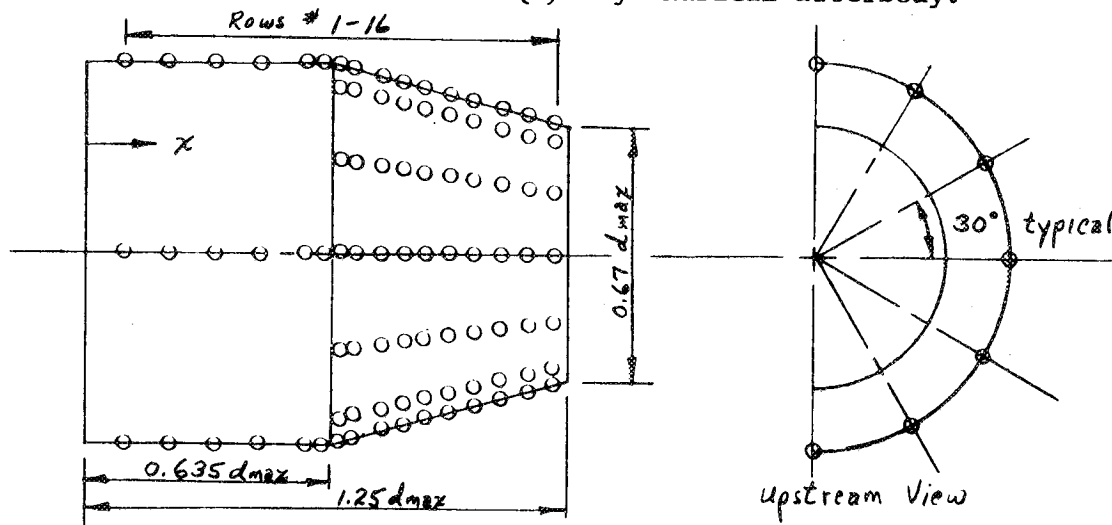
(b) Cylindrical body static pressures.

Figure 3. Concluded.





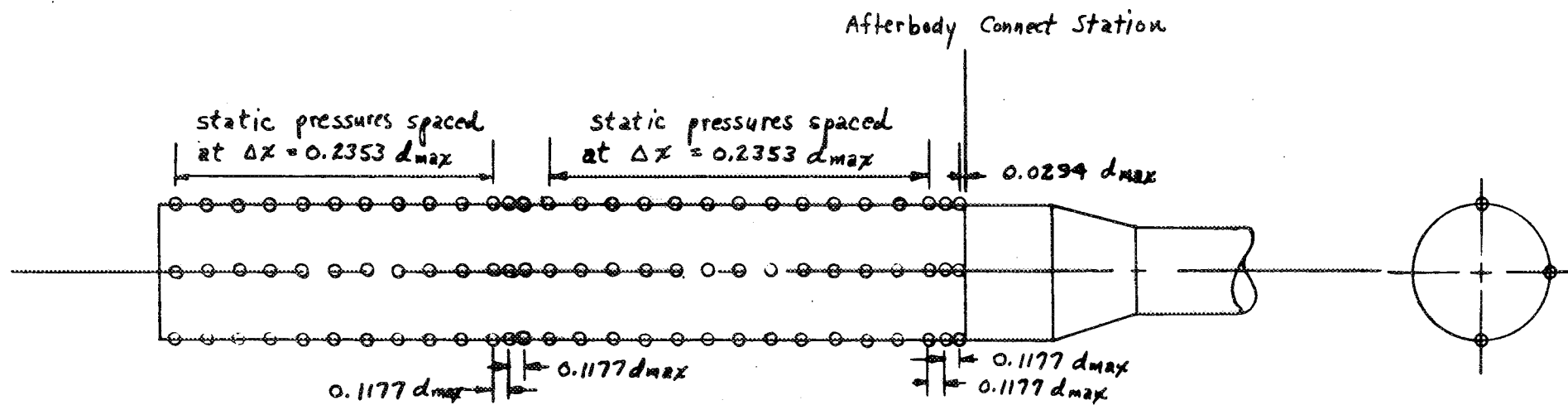
(b) Cylindrical afterbody.



(c) 15-degree conical boattail,  
 $r/d_{max} = 0$ .

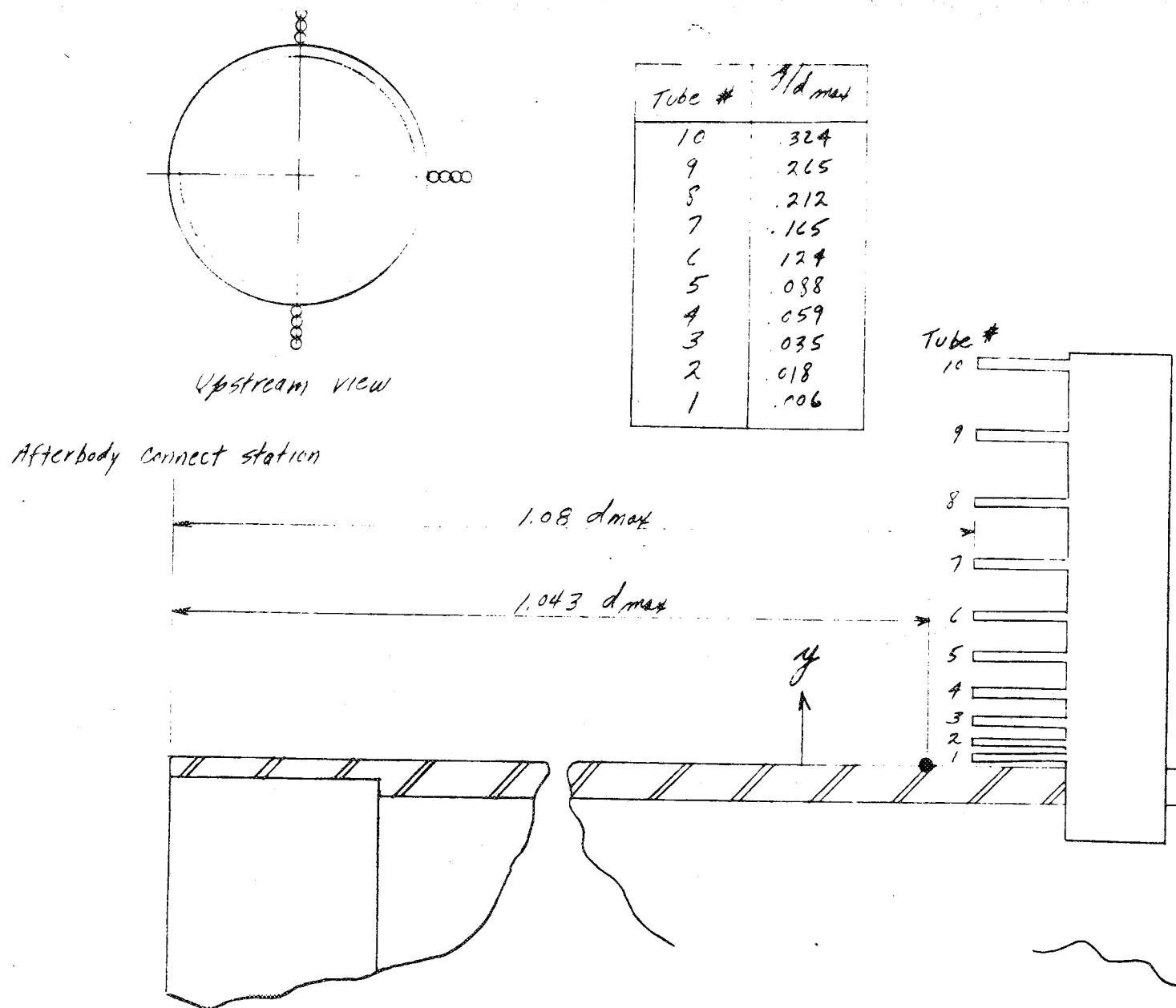
Row #	$x/d_{max}$
1	.103
2	.220
3	.338
4	.456
5	.574
6	.633
7	.668
8	.715
9	.773
10	.830
11	.885
12	.945
13	1.010
14	1.070
15	1.140
16	1.213

Figure 4. Continued.



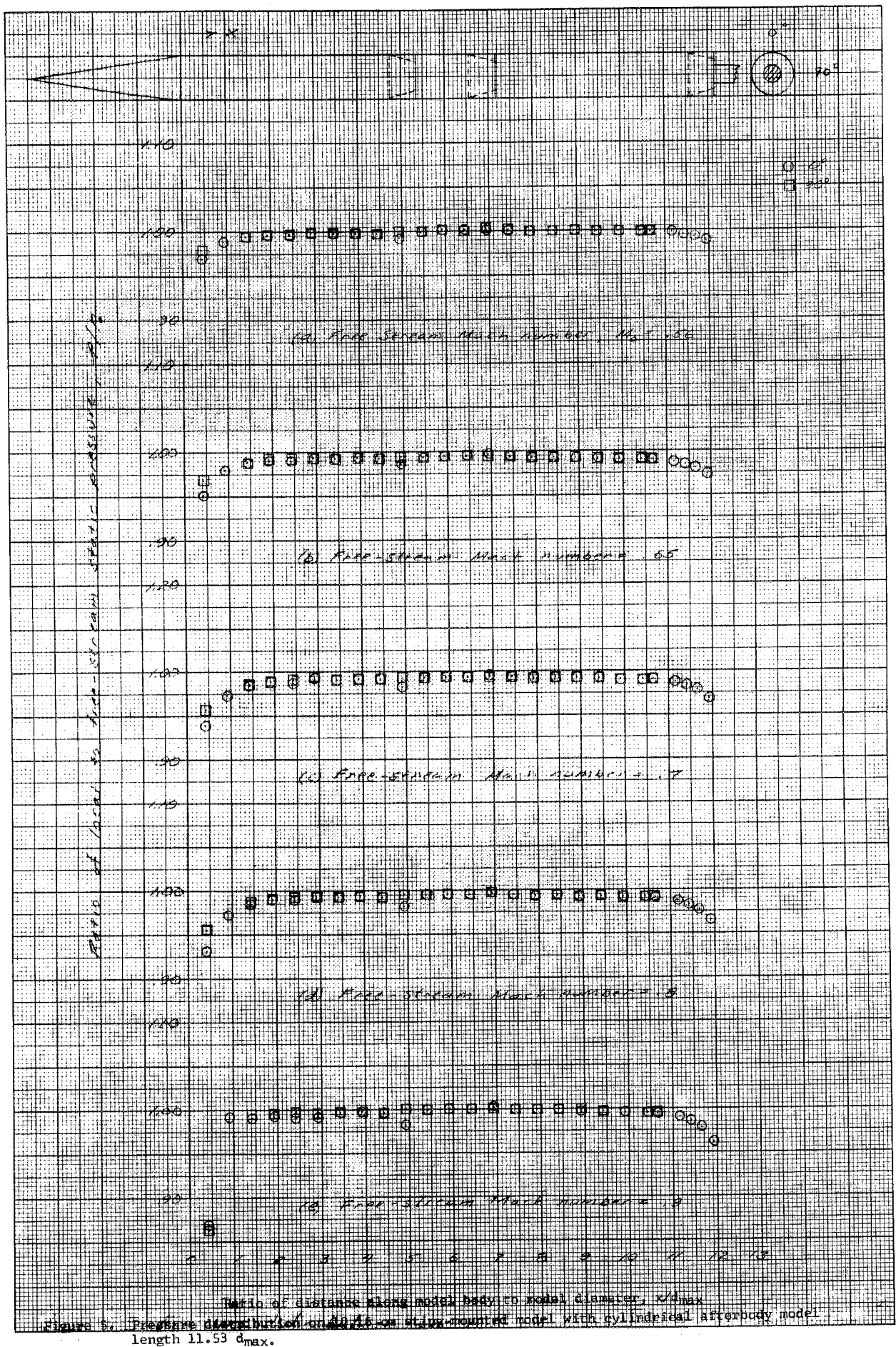
(d) Cylindrical body static pressures.

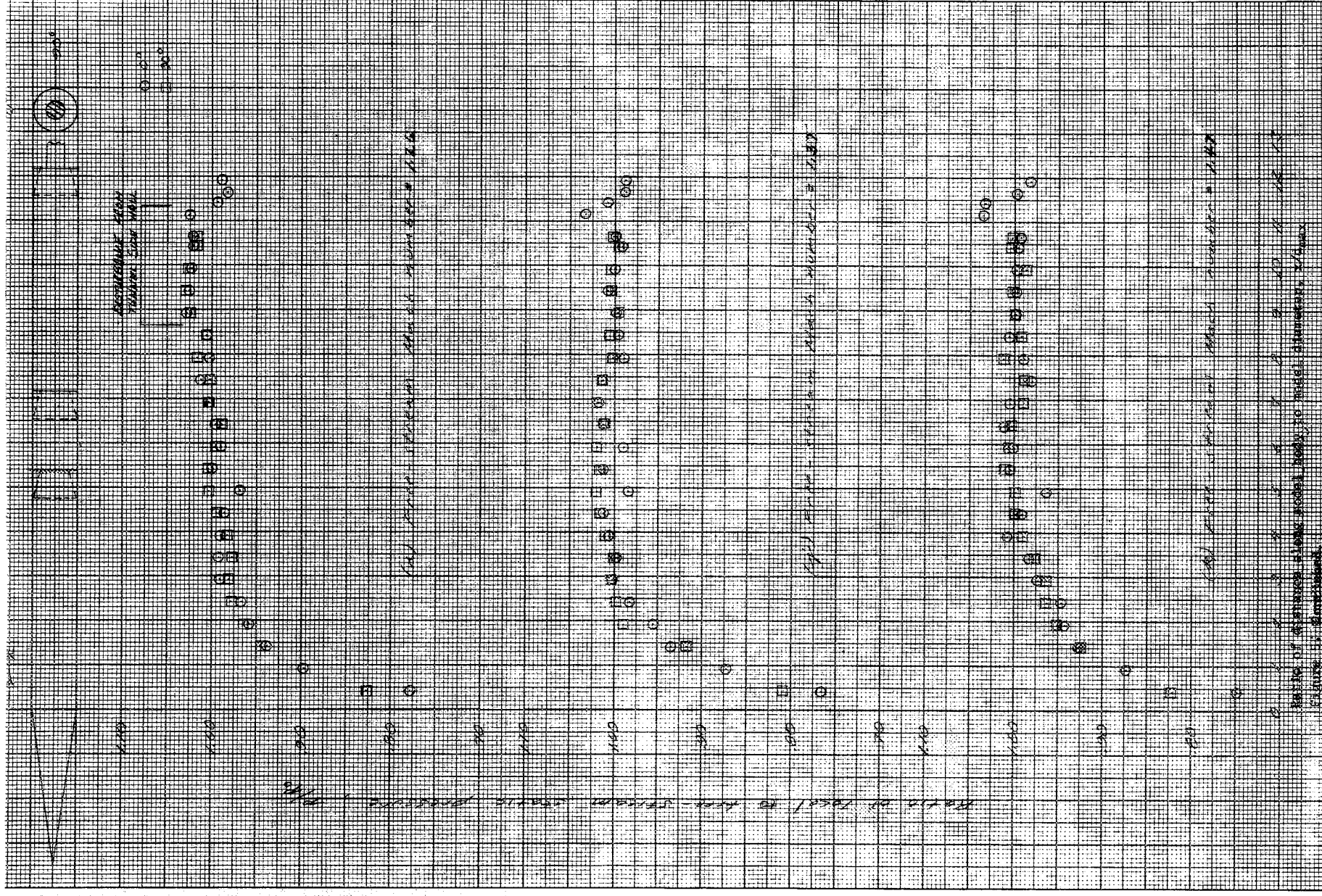
Figure 4. Continued.



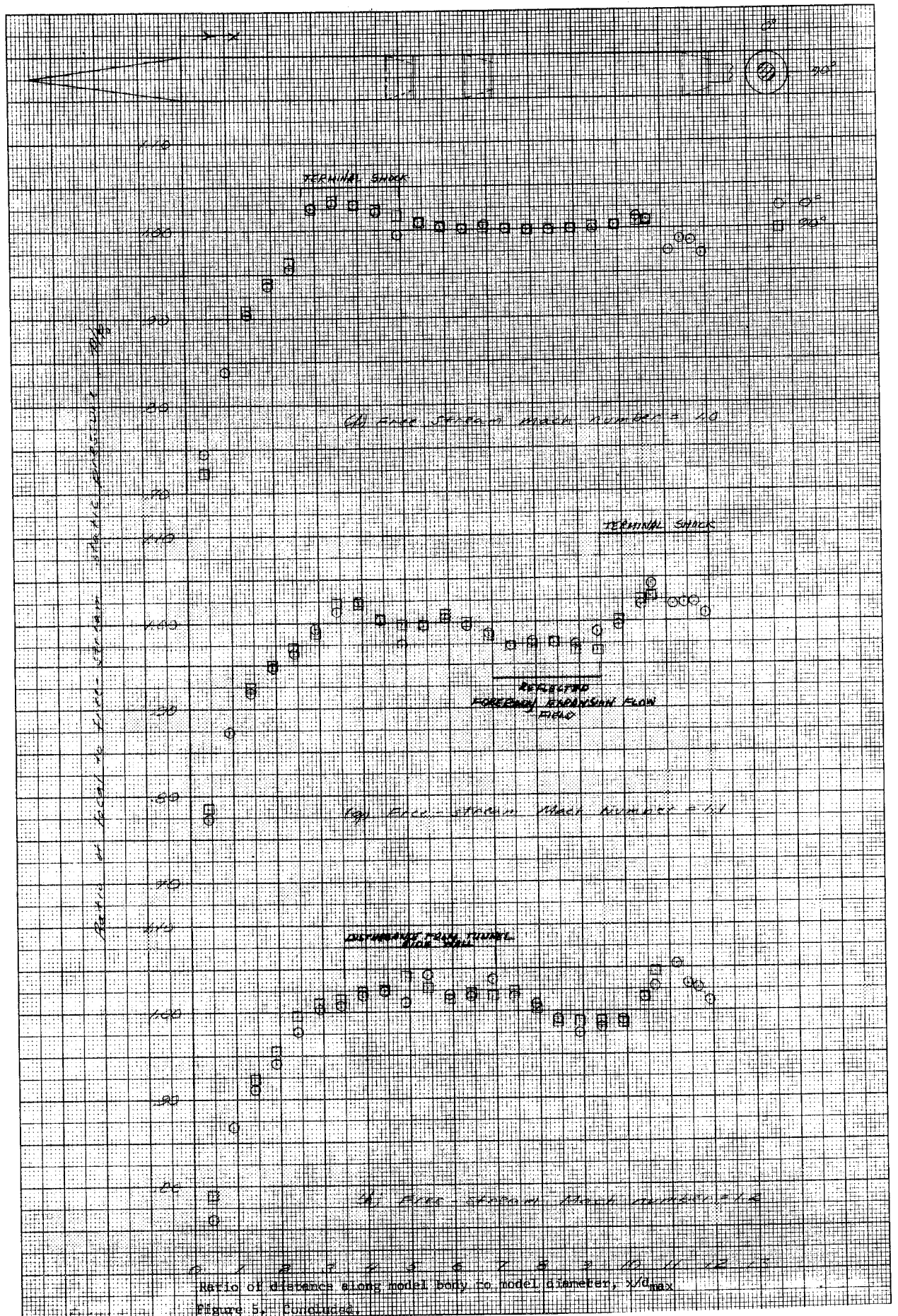
(e) Boundary-layer survey rakes.

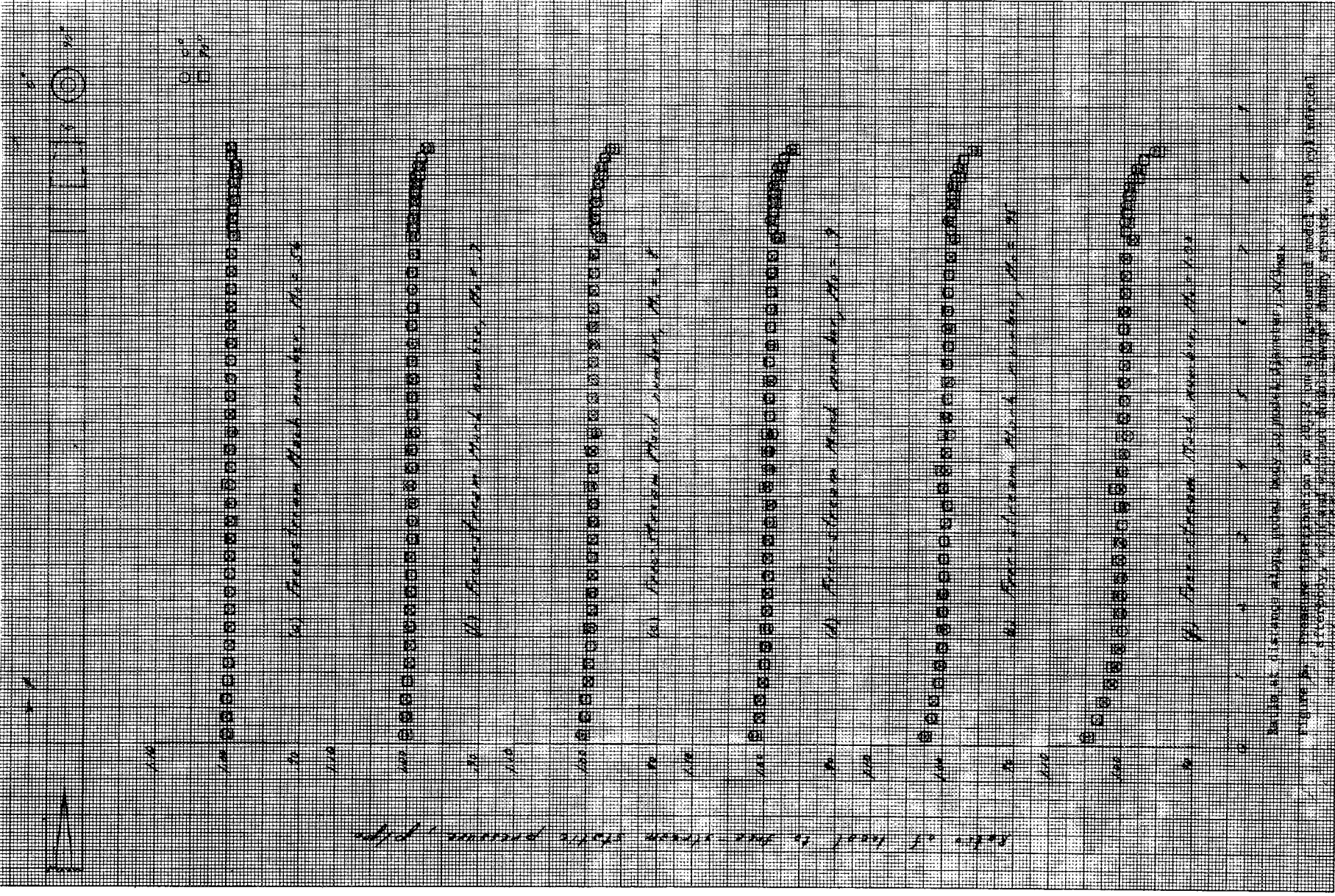
Figure 4. Concluded.











Ratio of head to free stream static pressure,  $p/p_{\infty}$

Figure 2. Pressure distribution on 20.7% thick airfoil model with 10% camber. At  $M_{\infty} = 0.5$ , the pressure distribution is shown for the airfoil model with 10% camber. At  $M_{\infty} = 1.5$ , the pressure distribution is shown for the airfoil model with 10% camber.



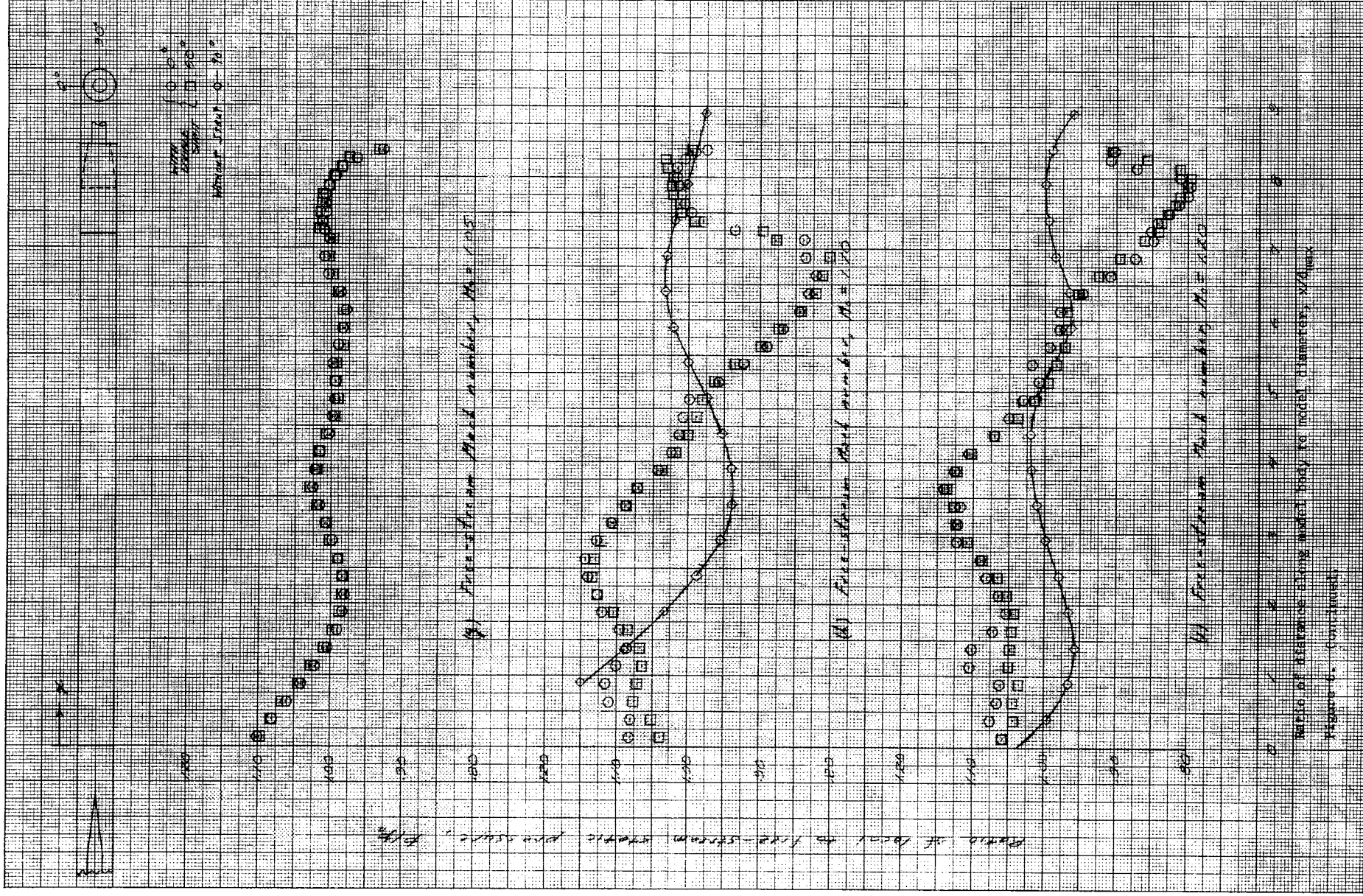
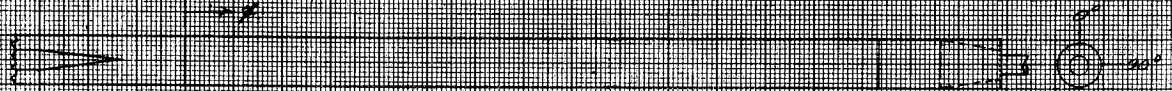
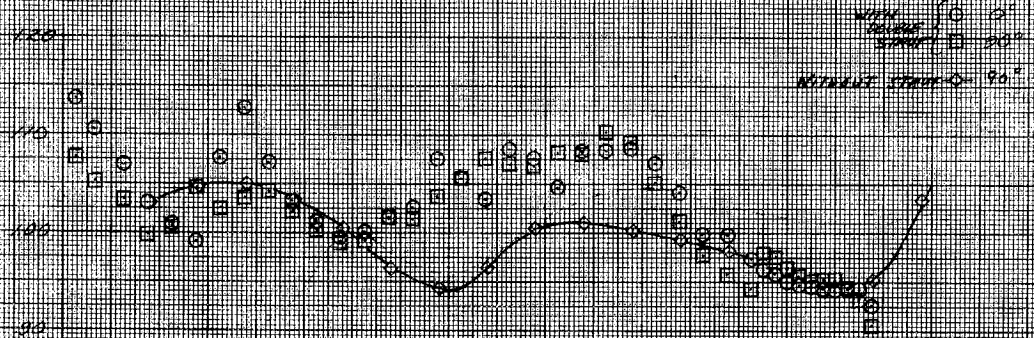


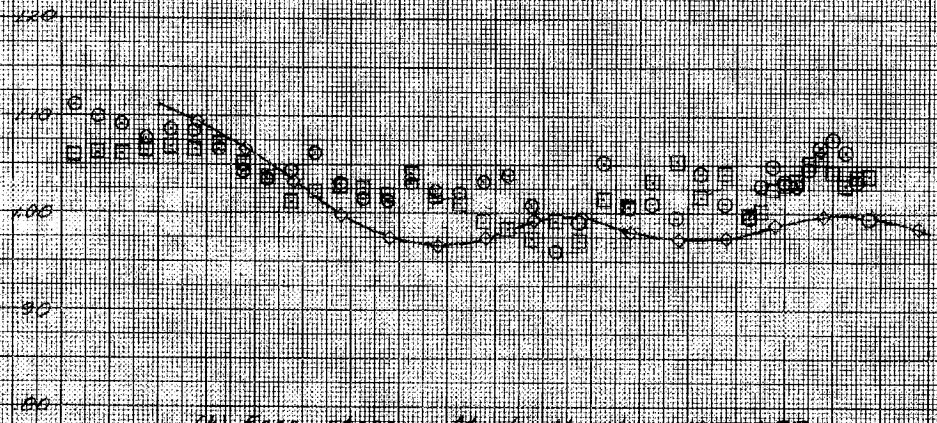
Figure 6. (continued)



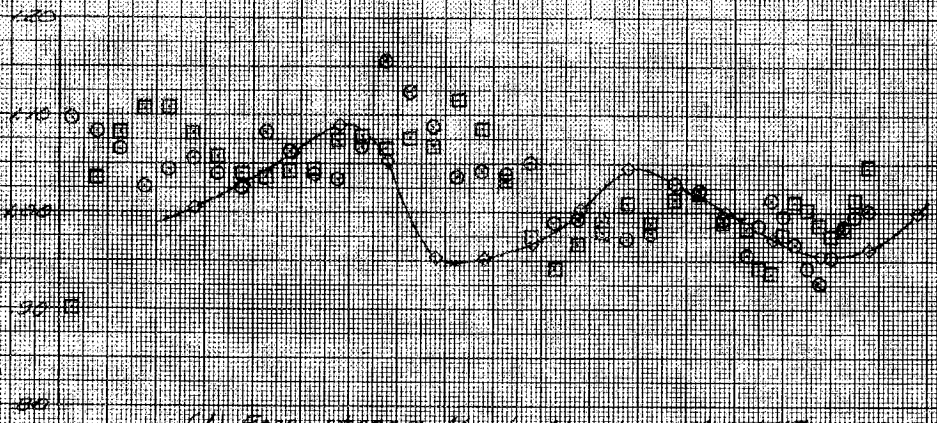
Ratio of local to free-stream static pressure,  $p/p_\infty$



(a) Free-stream Mach Number,  $M_\infty = 1.27$



(b) Free-stream Mach Number,  $M_\infty = 1.37$

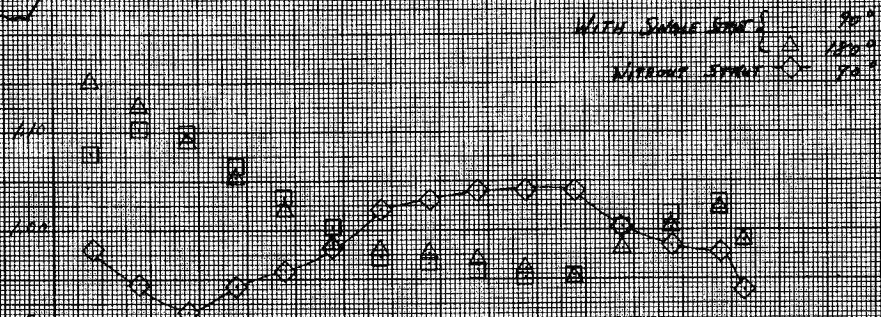
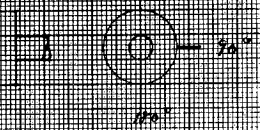


(c) Free-stream Mach Number,  $M_\infty = 1.47$

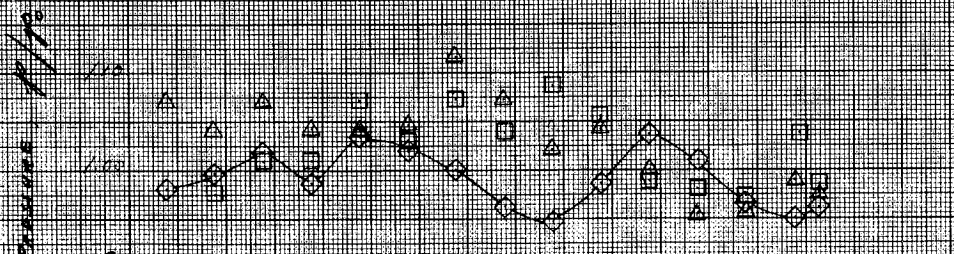
Ratio of distance along model body to model diameter,  $x/d_{max}$

Figure 6. Continued.

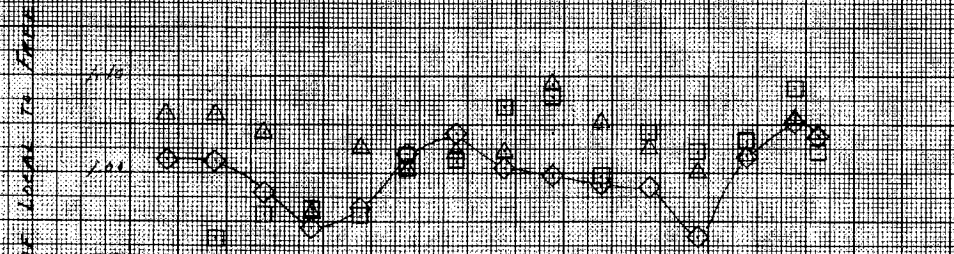




(a) Free-Stream Mach Number,  $M_\infty = 1.08$



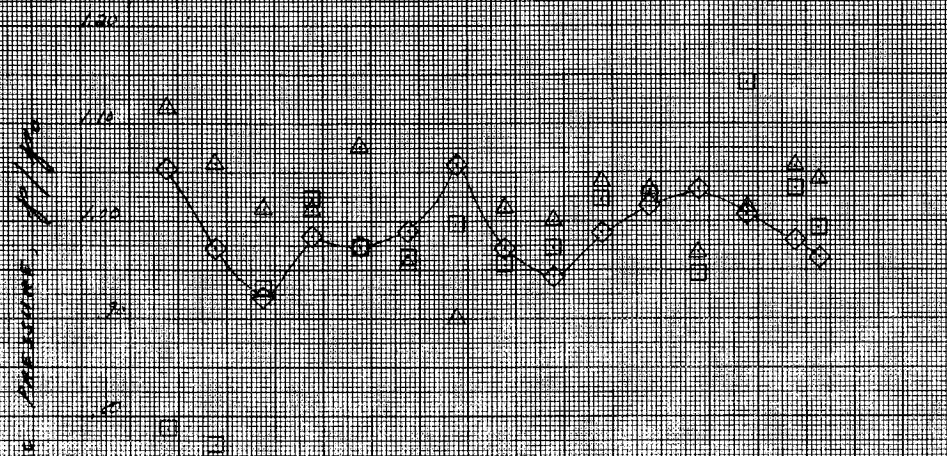
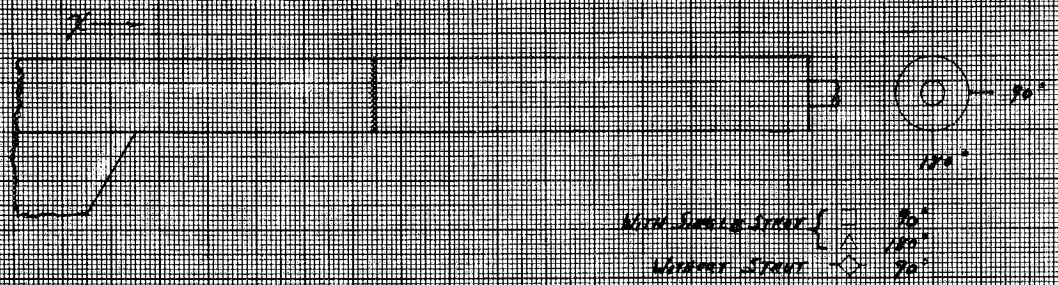
(b) Free-Stream Mach Number,  $M_\infty = 1.2$



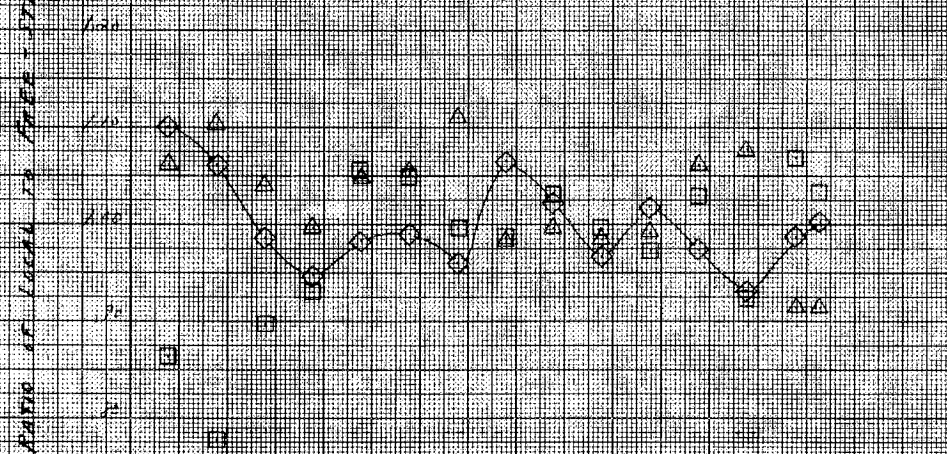
(c) Free-Stream Mach Number,  $M_\infty = 1.47$

Ratio of distance aft of forebody shoulder to model diameter,  $x/d_{max}$

Figure 7. Pressure distribution on 20.32 cm sting-mounted model with cylindrical afterbody, with and without single-sweep dummy strut.



(a) Free-Stream Mach Number,  $M_\infty = 1.31$

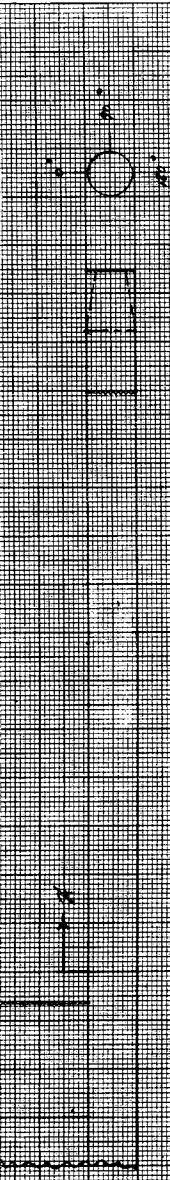


(b) Free-Stream Mach Number,  $M_\infty = 1.47$

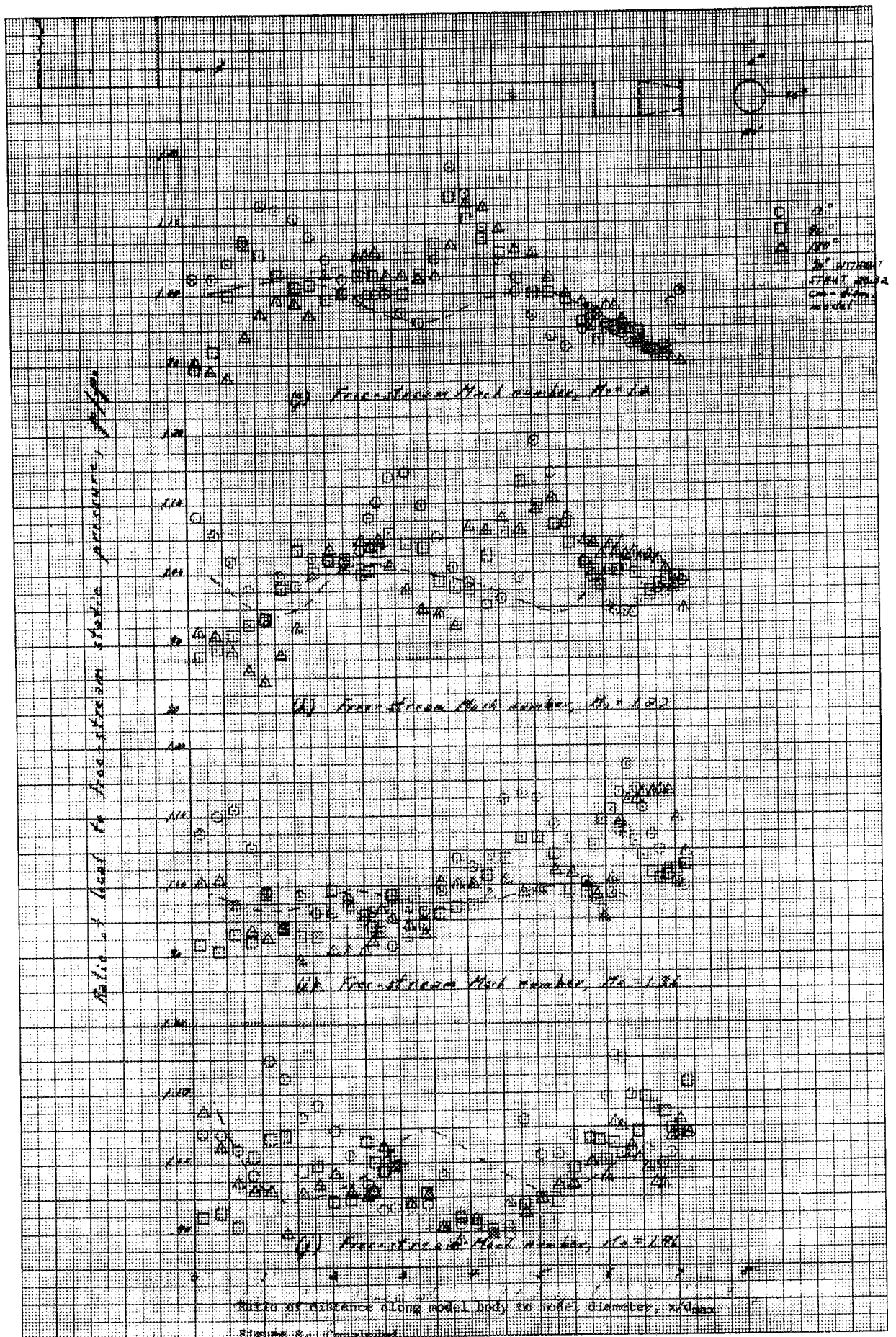
Ratio of distance aft of forebody shoulder to model diameter,  $x/d_{max}$

Figure 7. Concluded.





$\Delta$  0.1  
 $\square$  0.2  
 $\circ$  0.3  
 0.4  
 0.5  
 0.6  
 0.7  
 0.8  
 0.9  
 1.0  
 1.1  
 1.2  
 1.3  
 1.4  
 1.5  
 1.6  
 1.7  
 1.8  
 1.9  
 2.0  
 2.1  
 2.2  
 2.3  
 2.4  
 2.5  
 2.6  
 2.7  
 2.8  
 2.9  
 3.0  
 3.1  
 3.2  
 3.3  
 3.4  
 3.5  
 3.6  
 3.7  
 3.8  
 3.9  
 4.0  
 4.1  
 4.2  
 4.3  
 4.4  
 4.5  
 4.6  
 4.7  
 4.8  
 4.9  
 5.0  
 5.1  
 5.2  
 5.3  
 5.4  
 5.5  
 5.6  
 5.7  
 5.8  
 5.9  
 6.0  
 6.1  
 6.2  
 6.3  
 6.4  
 6.5  
 6.6  
 6.7  
 6.8  
 6.9  
 7.0  
 7.1  
 7.2  
 7.3  
 7.4  
 7.5  
 7.6  
 7.7  
 7.8  
 7.9  
 8.0  
 8.1  
 8.2  
 8.3  
 8.4  
 8.5  
 8.6  
 8.7  
 8.8  
 8.9  
 9.0  
 9.1  
 9.2  
 9.3  
 9.4  
 9.5  
 9.6  
 9.7  
 9.8  
 9.9  
 10.0  
 10.1  
 10.2  
 10.3  
 10.4  
 10.5  
 10.6  
 10.7  
 10.8  
 10.9  
 11.0  
 11.1  
 11.2  
 11.3  
 11.4  
 11.5  
 11.6  
 11.7  
 11.8  
 11.9  
 12.0  
 12.1  
 12.2  
 12.3  
 12.4  
 12.5  
 12.6  
 12.7  
 12.8  
 12.9  
 13.0  
 13.1  
 13.2  
 13.3  
 13.4  
 13.5  
 13.6  
 13.7  
 13.8  
 13.9  
 14.0  
 14.1  
 14.2  
 14.3  
 14.4  
 14.5  
 14.6  
 14.7  
 14.8  
 14.9  
 15.0  
 15.1  
 15.2  
 15.3  
 15.4  
 15.5  
 15.6  
 15.7  
 15.8  
 15.9  
 16.0  
 16.1  
 16.2  
 16.3  
 16.4  
 16.5  
 16.6  
 16.7  
 16.8  
 16.9  
 17.0  
 17.1  
 17.2  
 17.3  
 17.4  
 17.5  
 17.6  
 17.7  
 17.8  
 17.9  
 18.0  
 18.1  
 18.2  
 18.3  
 18.4  
 18.5  
 18.6  
 18.7  
 18.8  
 18.9  
 19.0  
 19.1  
 19.2  
 19.3  
 19.4  
 19.5  
 19.6  
 19.7  
 19.8  
 19.9  
 20.0  
 20.1  
 20.2  
 20.3  
 20.4  
 20.5  
 20.6  
 20.7  
 20.8  
 20.9  
 21.0  
 21.1  
 21.2  
 21.3  
 21.4  
 21.5  
 21.6  
 21.7  
 21.8  
 21.9  
 22.0  
 22.1  
 22.2  
 22.3  
 22.4  
 22.5  
 22.6  
 22.7  
 22.8  
 22.9  
 23.0  
 23.1  
 23.2  
 23.3  
 23.4  
 23.5  
 23.6  
 23.7  
 23.8  
 23.9  
 24.0  
 24.1  
 24.2  
 24.3  
 24.4  
 24.5  
 24.6  
 24.7  
 24.8  
 24.9  
 25.0  
 25.1  
 25.2  
 25.3  
 25.4  
 25.5  
 25.6  
 25.7  
 25.8  
 25.9  
 26.0  
 26.1  
 26.2  
 26.3  
 26.4  
 26.5  
 26.6  
 26.7  
 26.8  
 26.9  
 27.0  
 27.1  
 27.2  
 27.3  
 27.4  
 27.5  
 27.6  
 27.7  
 27.8  
 27.9  
 28.0  
 28.1  
 28.2  
 28.3  
 28.4  
 28.5  
 28.6  
 28.7  
 28.8  
 28.9  
 29.0  
 29.1  
 29.2  
 29.3  
 29.4  
 29.5  
 29.6  
 29.7  
 29.8  
 29.9  
 30.0  
 30.1  
 30.2  
 30.3  
 30.4  
 30.5  
 30.6  
 30.7  
 30.8  
 30.9  
 31.0  
 31.1  
 31.2  
 31.3  
 31.4  
 31.5  
 31.6  
 31.7  
 31.8  
 31.9  
 32.0  
 32.1  
 32.2  
 32.3  
 32.4  
 32.5  
 32.6  
 32.7  
 32.8  
 32.9  
 33.0  
 33.1  
 33.2  
 33.3  
 33.4  
 33.5  
 33.6  
 33.7  
 33.8  
 33.9  
 34.0  
 34.1  
 34.2  
 34.3  
 34.4  
 34.5  
 34.6  
 34.7  
 34.8  
 34.9  
 35.0  
 35.1  
 35.2  
 35.3  
 35.4  
 35.5  
 35.6  
 35.7  
 35.8  
 35.9  
 36.0  
 36.1  
 36.2  
 36.3  
 36.4  
 36.5  
 36.6  
 36.7  
 36.8  
 36.9  
 37.0  
 37.1  
 37.2  
 37.3  
 37.4  
 37.5  
 37.6  
 37.7  
 37.8  
 37.9  
 38.0  
 38.1  
 38.2  
 38.3  
 38.4  
 38.5  
 38.6  
 38.7  
 38.8  
 38.9  
 39.0  
 39.1  
 39.2  
 39.3  
 39.4  
 39.5  
 39.6  
 39.7  
 39.8  
 39.9  
 40.0  
 40.1  
 40.2  
 40.3  
 40.4  
 40.5  
 40.6  
 40.7  
 40.8  
 40.9  
 41.0  
 41.1  
 41.2  
 41.3  
 41.4  
 41.5  
 41.6  
 41.7  
 41.8  
 41.9  
 42.0  
 42.1  
 42.2  
 42.3  
 42.4  
 42.5  
 42.6  
 42.7  
 42.8  
 42.9  
 43.0  
 43.1  
 43.2  
 43.3  
 43.4  
 43.5  
 43.6  
 43.7  
 43.8  
 43.9  
 44.0  
 44.1  
 44.2  
 44.3  
 44.4  
 44.5  
 44.6  
 44.7  
 44.8  
 44.9  
 45.0  
 45.1  
 45.2  
 45.3  
 45.4  
 45.5  
 45.6  
 45.7  
 45.8  
 45.9  
 46.0  
 46.1  
 46.2  
 46.3  
 46.4  
 46.5  
 46.6  
 46.7  
 46.8  
 46.9  
 47.0  
 47.1  
 47.2  
 47.3  
 47.4  
 47.5  
 47.6  
 47.7  
 47.8  
 47.9  
 48.0  
 48.1  
 48.2  
 48.3  
 48.4  
 48.5  
 48.6  
 48.7  
 48.8  
 48.9  
 49.0  
 49.1  
 49.2  
 49.3  
 49.4  
 49.5  
 49.6  
 49.7  
 49.8  
 49.9  
 50.0  
 50.1  
 50.2  
 50.3  
 50.4  
 50.5  
 50.6  
 50.7  
 50.8  
 50.9  
 51.0  
 51.1  
 51.2  
 51.3  
 51.4  
 51.5  
 51.6  
 51.7  
 51.8  
 51.9  
 52.0  
 52.1  
 52.2  
 52.3  
 52.4  
 52.5  
 52.6  
 52.7  
 52.8  
 52.9  
 53.0  
 53.1  
 53.2  
 53.3  
 53.4  
 53.5  
 53.6  
 53.7  
 53.8  
 53.9  
 54.0  
 54.1  
 54.2  
 54.3  
 54.4  
 54.5  
 54.6  
 54.7  
 54.8  
 54.9  
 55.0  
 55.1  
 55.2  
 55.3  
 55.4  
 55.5  
 55.6  
 55.7  
 55.8  
 55.9  
 56.0  
 56.1  
 56.2  
 56.3  
 56.4  
 56.5  
 56.6  
 56.7  
 56.8  
 56.9  
 57.0  
 57.1  
 57.2  
 57.3  
 57.4  
 57.5  
 57.6  
 57.7  
 57.8  
 57.9  
 58.0  
 58.1  
 58.2  
 58.3  
 58.4  
 58.5  
 58.6  
 58.7  
 58.8  
 58.9  
 59.0  
 59.1  
 59.2  
 59.3  
 59.4  
 59.5  
 59.6  
 59.7  
 59.8  
 59.9  
 60.0  
 60.1  
 60.2  
 60.3  
 60.4  
 60.5  
 60.6  
 60.7  
 60.8  
 60.9  
 61.0  
 61.1  
 61.2  
 61.3  
 61.4  
 61.5  
 61.6  
 61.7  
 61.8  
 61.9  
 62.0  
 62.1  
 62.2  
 62.3  
 62.4  
 62.5  
 62.6  
 62.7  
 62.8  
 62.9  
 63.0  
 63.1  
 63.2  
 63.3  
 63.4  
 63.5  
 63.6  
 63.7  
 63.8  
 63.9  
 64.0  
 64.1  
 64.2  
 64.3  
 64.4  
 64.5  
 64.6  
 64.7  
 64.8  
 64.9  
 65.0  
 65.1  
 65.2  
 65.3  
 65.4  
 65.5  
 65.6  
 65.7  
 65.8  
 65.9  
 66.0  
 66.1  
 66.2  
 66.3  
 66.4  
 66.5  
 66.6  
 66.7  
 66.8  
 66.9  
 67.0  
 67.1  
 67.2  
 67.3  
 67.4  
 67.5  
 67.6  
 67.7  
 67.8  
 67.9  
 68.0  
 68.1  
 68.2  
 68.3  
 68.4  
 68.5  
 68.6  
 68.7  
 68.8  
 68.9  
 69.0  
 69.1  
 69.2  
 69.3  
 69.4  
 69.5  
 69.6  
 69.7  
 69.8  
 69.9  
 70.0  
 70.1  
 70.2  
 70.3  
 70.4  
 70.5  
 70.6  
 70.7  
 70.8  
 70.9  
 71.0  
 71.1  
 71.2  
 71.3  
 71.4  
 71.5  
 71.6  
 71.7  
 71.8  
 71.9  
 72.0  
 72.1  
 72.2  
 72.3  
 72.4  
 72.5  
 72.6  
 72.7  
 72.8  
 72.9  
 73.0  
 73.1  
 73.2  
 73.3  
 73.4  
 73.5  
 73.6  
 73.7  
 73.8  
 73.9  
 74.0  
 74.1  
 74.2  
 74.3  
 74.4  
 74.5  
 74.6  
 74.7  
 74.8  
 74.9  
 75.0  
 75.1  
 75.2  
 75.3  
 75.4  
 75.5  
 75.6  
 75.7  
 75.8  
 75.9  
 76.0  
 76.1  
 76.2  
 76.3  
 76.4  
 76.5  
 76.6  
 76.7  
 76.8  
 76.9  
 77.0  
 77.1  
 77.2  
 77.3  
 77.4  
 77.5  
 77.6  
 77.7  
 77.8  
 77.9  
 78.0  
 78.1  
 78.2  
 78.3  
 78.4  
 78.5  
 78.6  
 78.7  
 78.8  
 78.9  
 79.0  
 79.1  
 79.2  
 79.3  
 79.4  
 79.5  
 79.6  
 79.7  
 79.8  
 79.9  
 80.0  
 80.1  
 80.2  
 80.3  
 80.4  
 80.5  
 80.6  
 80.7  
 80.8  
 80.9  
 81.0  
 81.1  
 81.2  
 81.3  
 81.4  
 81.5  
 81.6  
 81.7  
 81.8  
 81.9  
 82.0  
 82.1  
 82.2  
 82.3  
 82.4  
 82.5  
 82.6  
 82.7  
 82.8  
 82.9  
 83.0  
 83.1  
 83.2  
 83.3  
 83.4  
 83.5  
 83.6  
 83.7  
 83.8  
 83.9  
 84.0  
 84.1  
 84.2  
 84.3  
 84.4  
 84.5  
 84.6  
 84.7  
 84.8  
 84.9  
 85.0  
 85.1  
 85.2  
 85.3  
 85.4  
 85.5  
 85.6  
 85.7  
 85.8  
 85.9  
 86.0  
 86.1  
 86.2  
 86.3  
 86.4  
 86.5  
 86.6  
 86.7  
 86.8  
 86.9  
 87.0  
 87.1  
 87.2  
 87.3  
 87.4  
 87.5  
 87.6  
 87.7  
 87.8  
 87.9  
 88.0  
 88.1  
 88.2  
 88.3  
 88.4  
 88.5  
 88.6  
 88.7  
 88.8  
 88.9  
 89.0  
 89.1  
 89.2  
 89.3  
 89.4  
 89.5  
 89.6  
 89.7  
 89.8  
 89.9  
 90.0  
 90.1  
 90.2  
 90.3  
 90.4  
 90.5  
 90.6  
 90.7  
 90.8  
 90.9  
 91.0  
 91.1  
 91.2  
 91.3  
 91.4  
 91.5  
 91.6  
 91.7  
 91.8  
 91.9  
 92.0  
 92.1  
 92.2  
 92.3  
 92.4  
 92.5  
 92.6  
 92.7  
 92.8  
 92.9  
 93.0  
 93.1  
 93.2  
 93.3  
 93.4  
 93.5  
 93.6  
 93.7  
 93.8  
 93.9  
 94.0  
 94.1  
 94.2  
 94.3  
 94.4  
 94.5  
 94.6  
 94.7  
 94.8  
 94.9  
 95.0  
 95.1  
 95.2  
 95.3  
 95.4  
 95.5  
 95.6  
 95.7  
 95.8  
 95.9  
 96.0  
 96.1  
 96.2  
 96.3  
 96.4  
 96.5  
 96.6  
 96.7  
 96.8  
 96.9  
 97.0  
 97.1  
 97.2  
 97.3  
 97.4  
 97.5  
 97.6  
 97.7  
 97.8  
 97.9  
 98.0  
 98.1  
 98.2  
 98.3  
 98.4  
 98.5  
 98.6  
 98.7  
 98.8  
 98.9  
 99.0  
 99.1  
 99.2  
 99.3  
 99.4  
 99.5  
 99.6  
 99.7  
 99.8  
 99.9  
 100.0  
 100.1  
 100.2  
 100.3  
 100.4  
 100.5  
 100.6  
 100.7  
 100.8  
 100.9  
 101.0  
 101.1  
 101.2  
 101.3  
 101.4  
 101.5  
 101.6  
 101.7  
 101.8  
 101.9  
 102.0  
 102.1  
 102.2  
 102.3  
 102.4  
 102.5  
 102.6  
 102.7  
 102.8  
 102.9  
 103.0  
 103.1  
 103.2  
 103.3  
 103.4  
 103.5  
 103.6  
 103.7  
 103.8  
 103.9  
 104.0  
 104.1  
 104.2  
 104.3  
 104.4  
 104.5  
 104.6  
 104.7  
 104.8  
 104.9  
 105.0  
 105.1  
 105.2  
 105.3  
 105.4  
 105.5  
 105.6  
 105.7  
 105.8  
 105.9  
 106.0  
 106.1  
 106.2  
 106.3  
 106.4  
 106.5  
 106.6  
 106.7  
 106.8  
 106.9  
 107.0  
 107.1  
 107.2  
 107.3  
 107.4  
 107.5  
 107.6  
 107.7  
 107.8  
 107.9  
 108.0  
 108.1  
 108.2  
 108.3  
 108.4  
 108.5  
 108.6  
 108.7  
 108.8  
 108.9  
 109.0  
 109.1  
 109.2  
 109.3  
 109.4  
 109.5  
 109.6  
 109.7  
 109.8  
 109.9  
 110.0  
 110.1  
 110.2  
 110.3  
 110.4  
 110.5  
 110.6  
 110.7  
 110.8  
 110.9  
 111.0  
 111.1  
 111.2  
 111.3  
 111.4  
 111.5  
 111.6  
 111.7  
 111.8  
 111.9  
 112.0  
 112.1  
 112.2  
 112.3  
 112.4  
 112.5  
 112.6  
 112.7  
 112.8  
 112.9  
 113.0  
 113.1  
 113.2  
 113.3  
 113.4  
 113.5  
 113.6  
 113.7  
 113.8  
 113.9  
 114.0  
 114.1  
 114.2  
 114.3  
 114.4  
 114.5  
 114.6  
 114.7  
 114.8  
 114.9  
 115.0  
 115.1  
 115.2  
 115.3  
 115.4  
 115.5  
 115.6  
 115.7  
 115.8  
 115.9  
 116.0  
 116.1  
 116.2  
 116.3  
 116.4  
 116.5  
 116.6  
 116.7  
 116.8  
 116.9  
 117.0  
 117.1  
 117.2  
 117.3  
 117.4  
 117.5  
 117.6  
 117.7  
 117.8  
 117.9  
 118.0  
 118.1  
 118.2  
 118.3  
 118.4  
 118.5  
 118.6  
 118.7  
 118.8  
 118.9  
 119.0  
 119.1  
 119.2  
 119.3  
 119.4  
 119.5  
 119.6  
 119.7  
 119.8  
 119.9  
 120.0  
 120.1  
 120.2  
 120.3  
 120.4  
 120.5  
 120.6  
 120.7  
 120.8  
 120.9  
 121.0  
 121.1  
 121.2  
 121.3  
 121.4  
 121.5  
 121.6  
 121.7  
 121.8  
 121.9  
 122.0  
 122.1  
 122.2  
 122.3  
 122.4  
 122.5  
 122.6  
 122.7  
 122.8  
 122.9  
 123.0  
 123.1  
 123.2  
 123.3  
 123.4  
 123.5  
 123.6  
 123.7  
 123.8  
 123.9  
 124.0  
 124.1  
 124.2  
 124.3  
 124.4  
 124.5  
 124.6  
 124.7  
 124.8  
 124.9  
 125.0  
 125.1  
 125.2  
 125.3  
 125.4  
 125.5  
 125.6  
 125.7  
 125.8  
 125.9  
 126.0  
 126.1  
 126.2  
 126.3  
 126.4  
 126.5  
 126.6  
 126.7  
 126.8  
 126.9  
 127.0  
 127.1  
 127.2  
 127.3  
 127.4  
 127.5  
 127.6  
 127.7  
 127.8  
 127.9  
 128.0  
 128.1  
 128.2  
 128.3  
 128.4  
 128.5  
 128.6  
 128.7  
 128.8  
 128.9  
 129.0  
 129.1  
 129.2  
 129.3  
 129.4  
 129.5  
 129.6  
 129.7  
 129.8  
 129.9  
 130.0  
 130.1  
 130.2  
 130.3  
 130.4  
 130.5  
 130.6  
 130.7  
 130.8  
 130.9  
 131.0  
 131.1  
 131.2  
 131.3  
 131.4  
 131.5  
 131.6  
 131.7  
 131.8  
 131.9  
 132.0  
 132.1  
 132.2  
 132.3  
 132.4  
 132.5  
 132.6  
 132.7  
 132.8  
 132.9  
 133.0  
 133.1  
 133.2





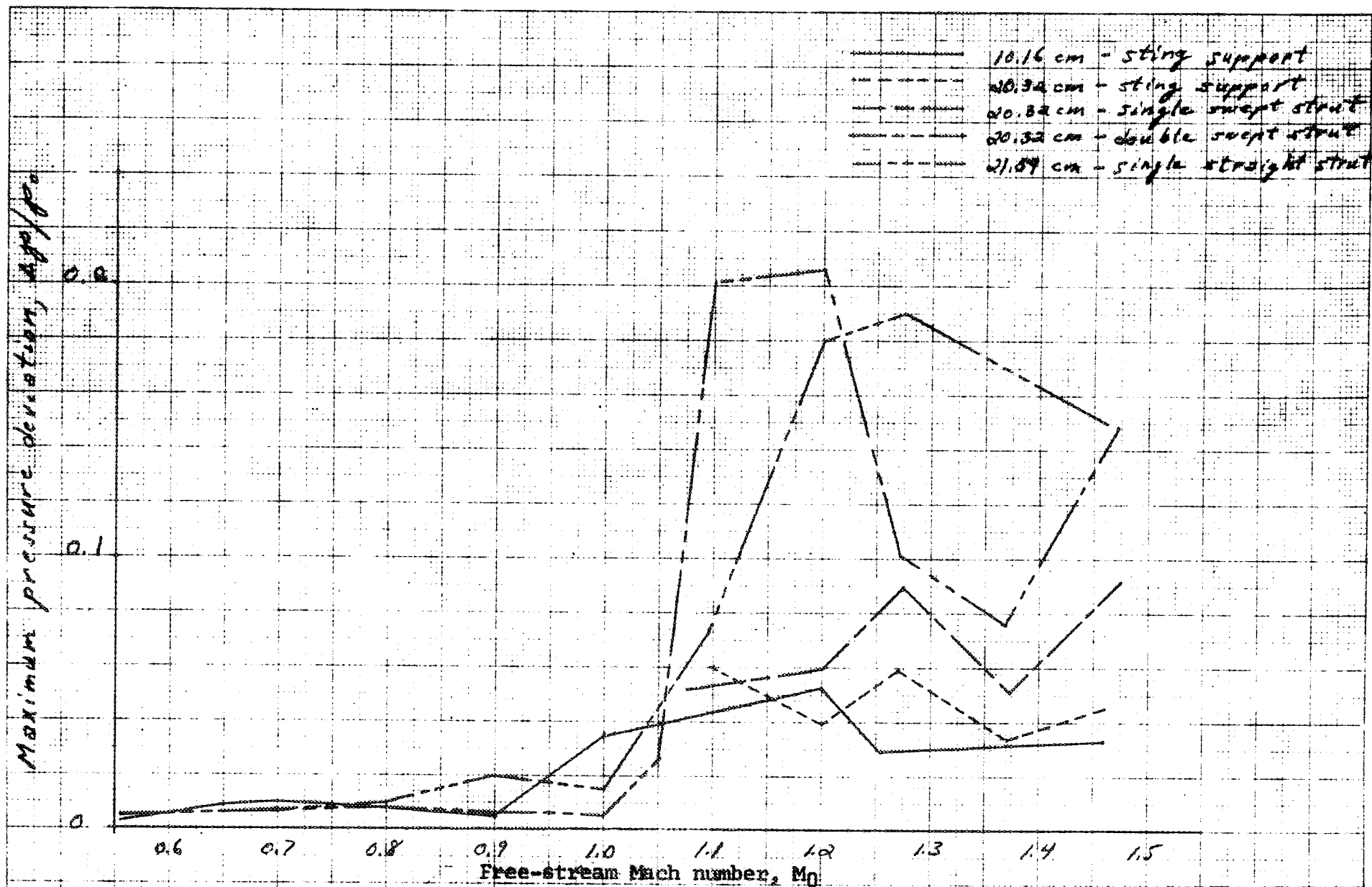


Figure 9. Summary of maximum pressure deviation for all models investigated.

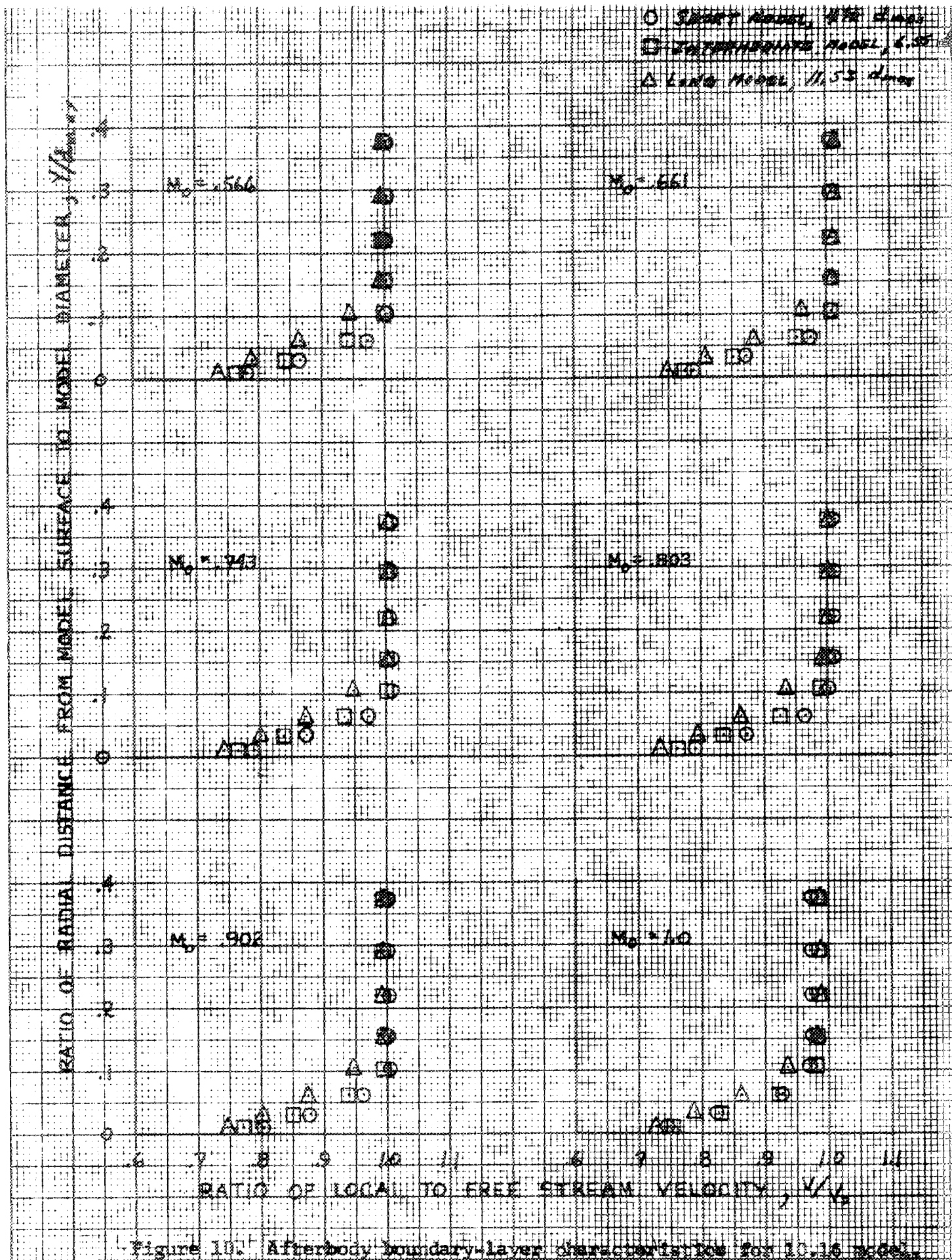


Figure 10. Afterbody boundary-layer characteristics for 10.16 model.

RATIO OF RADIAL DISTANCE FROM MODEL SURFACE TO MODEL DIAMETER,  $Y/d_{max}$

- SMART MODEL, 4.72  $d_{max}$
- INTERMEDIATE MODEL, 6.35  $d_{max}$
- △ LONG MODEL, 11.53  $d_{max}$

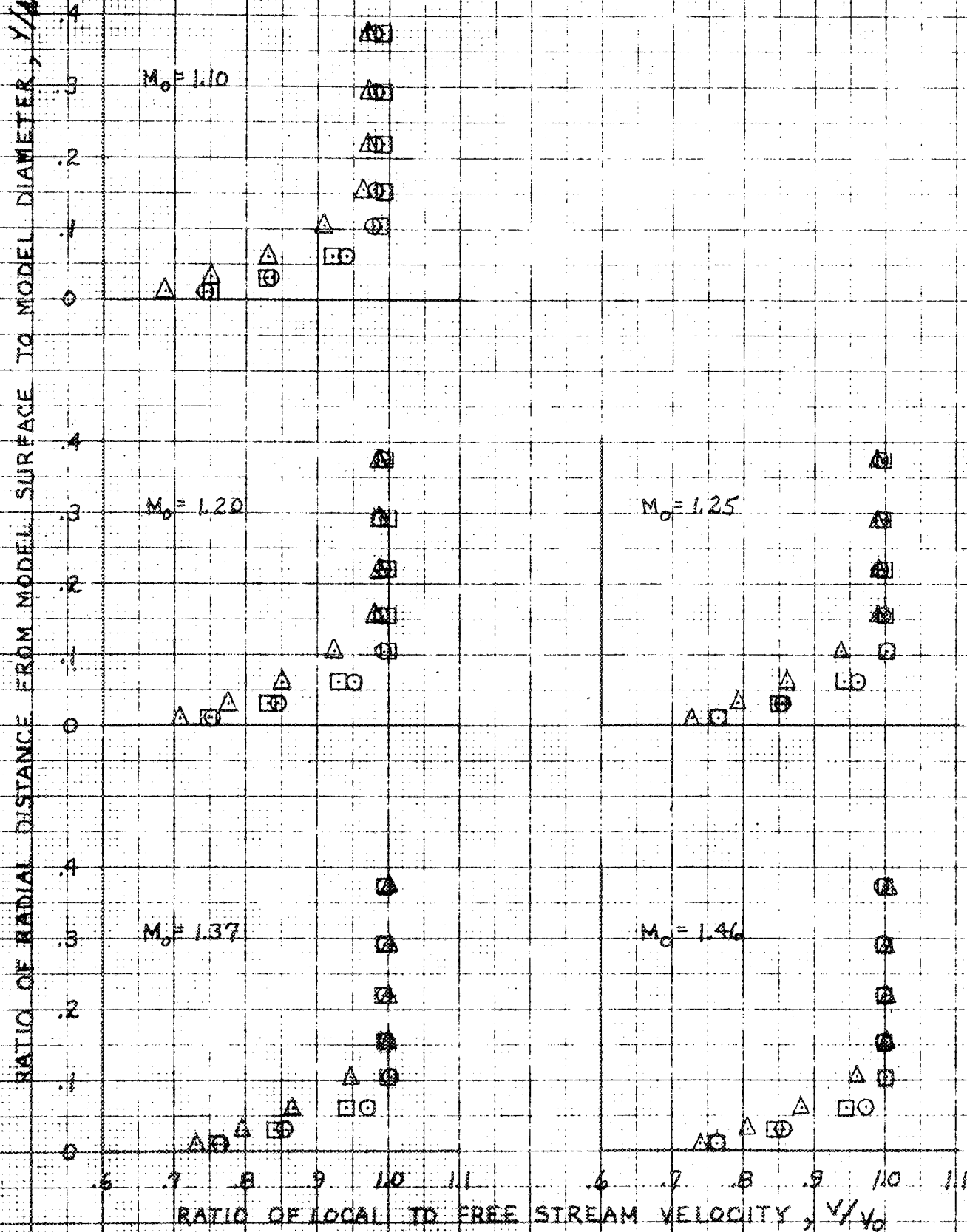


Figure 10. Concluded.

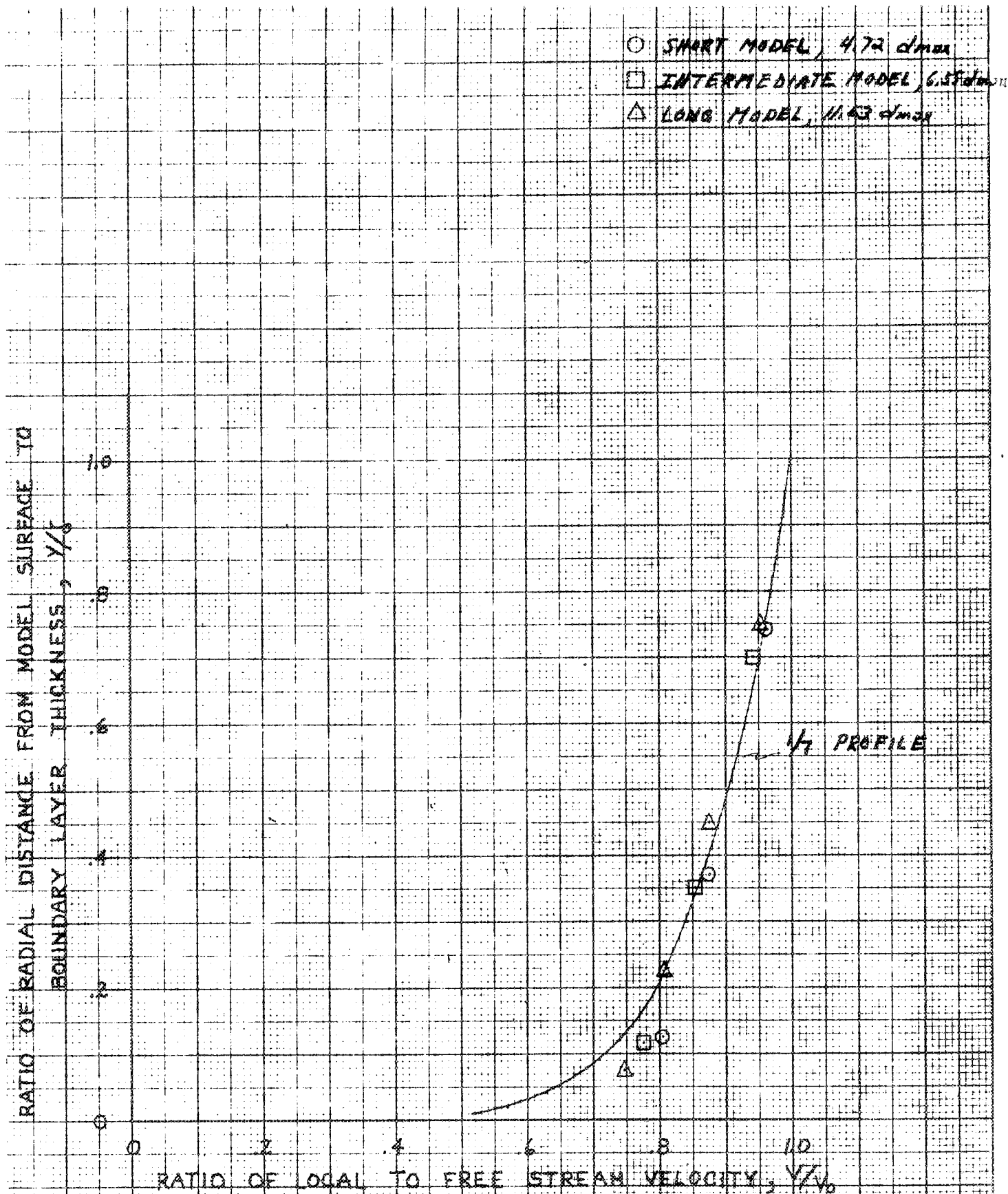


Figure 11. Typical boundary-layer profile for 19.15 cm model, free-stream Mach number 0.9.

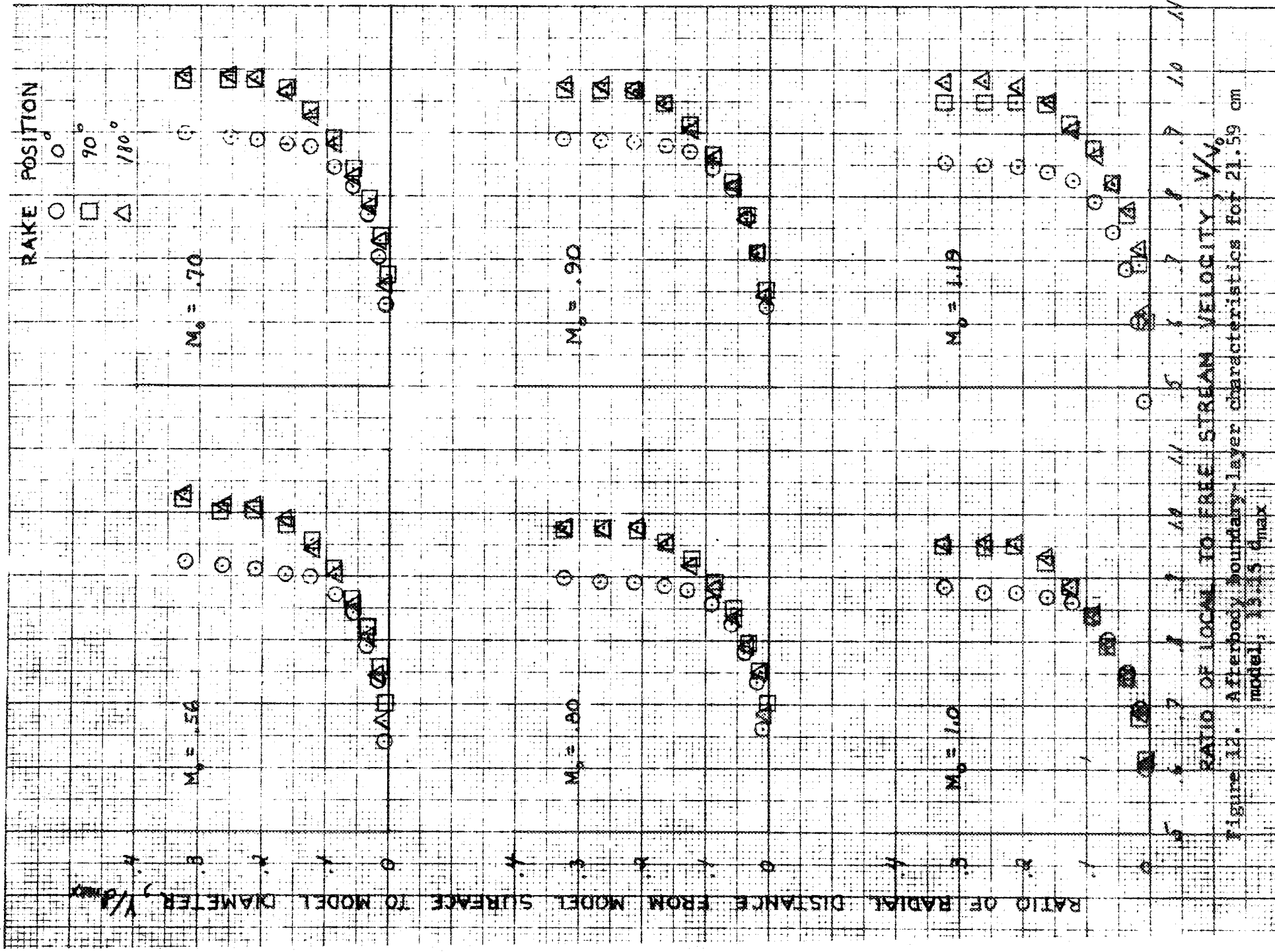


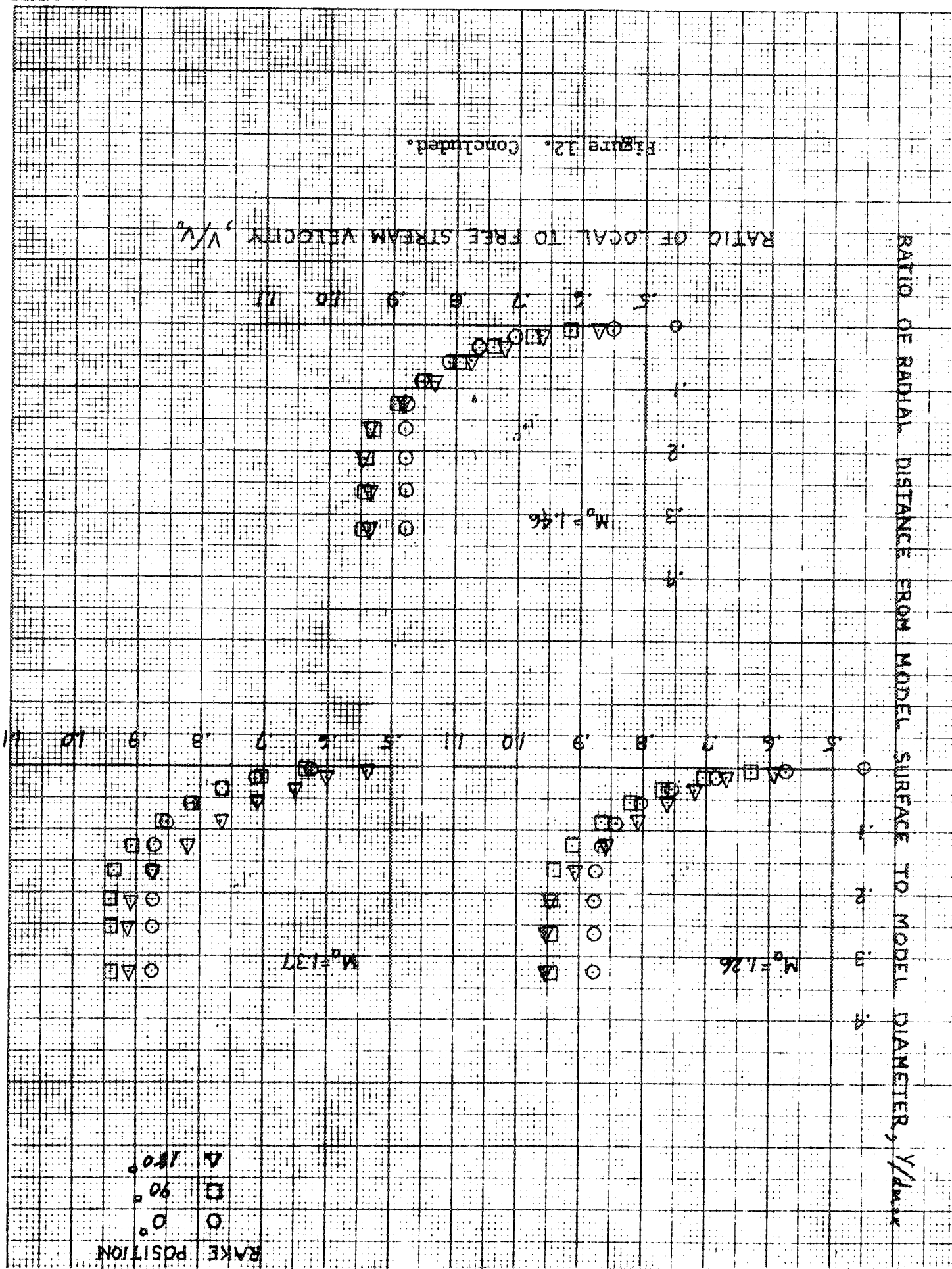
Figure 12. Afterbody boundary-layer characteristics for 21.59 cm model,  $15.15^\circ$  max.

RATIO OF RADIAL DISTANCE FROM MODEL SURFACE TO MODEL DIAMETER,  $y/d_{max}$

RATIO OF LOCAL TO FREE STREAM VELOCITY,  $V/V_\infty$

Figure 12. Concluded.

RAKE POSITION  
 $\Delta$  180°  
 $\square$  90°  
 $\circ$  0°





RATIO OF RADIAL DISTANCE FROM MODEL SURFACE TO  
BOUNDARY LAYER THICKNESS,  $y/\delta$

RATIO OF LOCAL TO FREE STREAM VELOCITY,  $V/V_\infty$

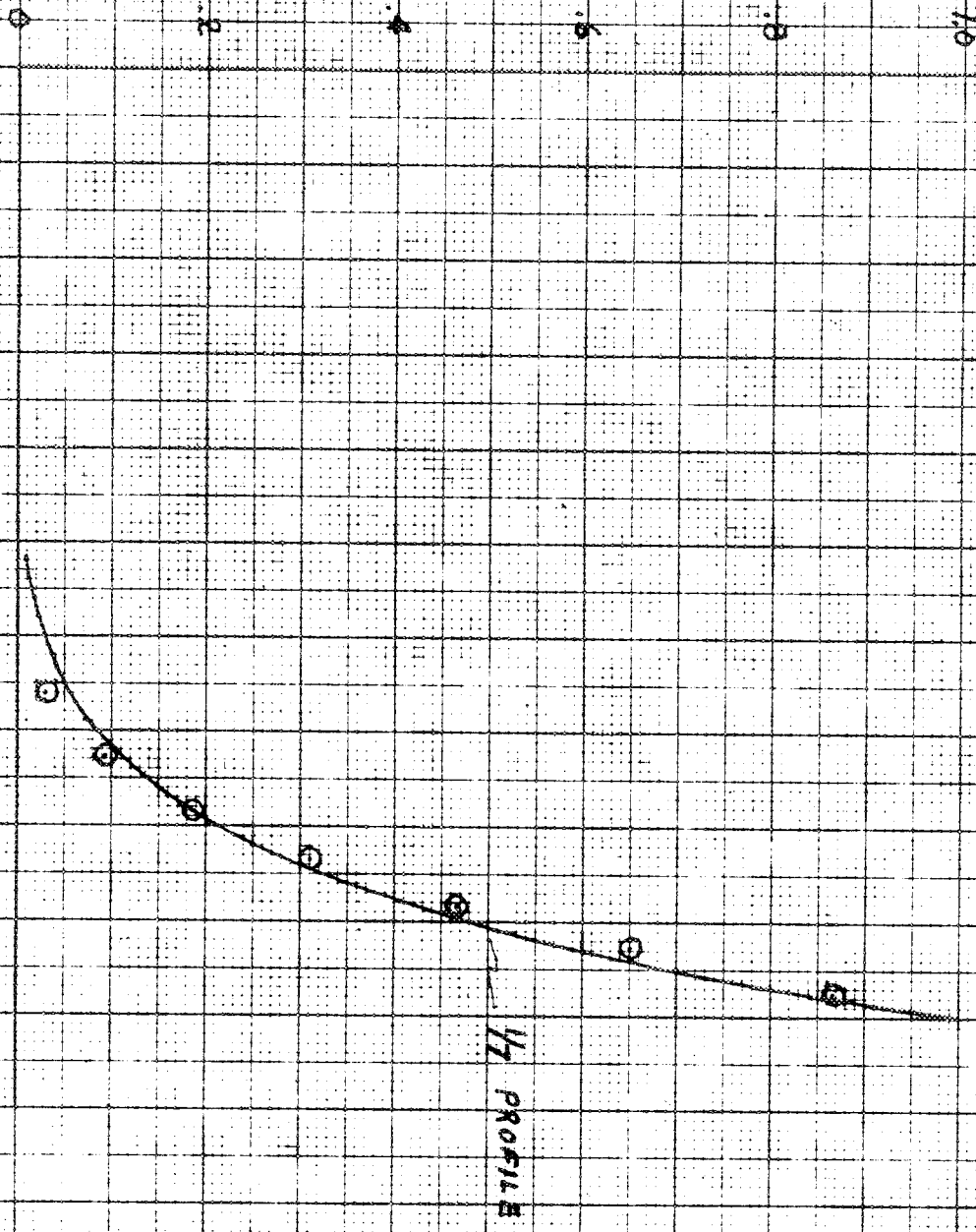


Figure 13. Typical boundary layer profile for 21.59 cm model; free-stream Mach number 0.9; rake position 180 deg.

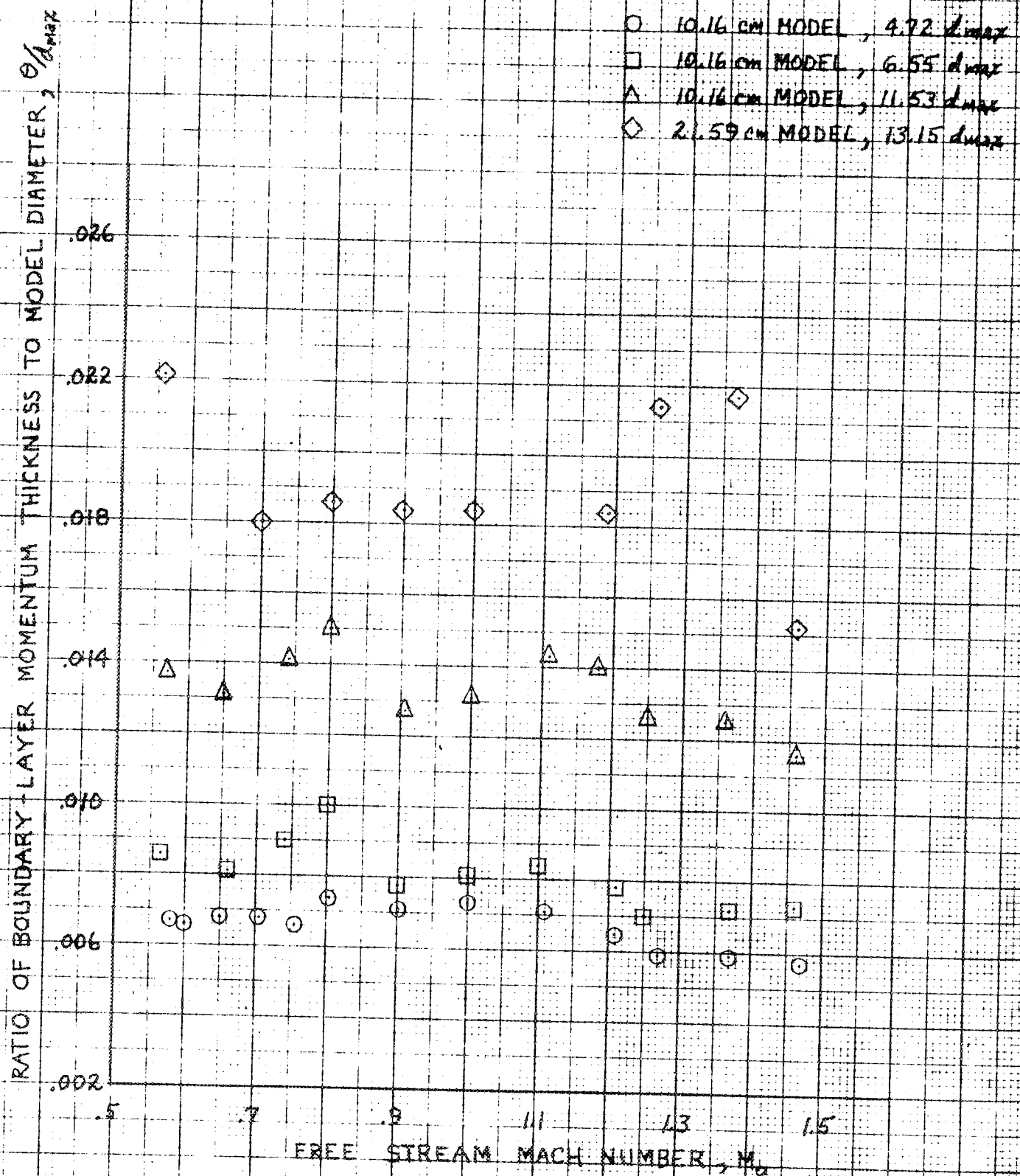


Figure 14. Boundary-layer momentum thickness for 10.16 cm and 21.59 cm models.



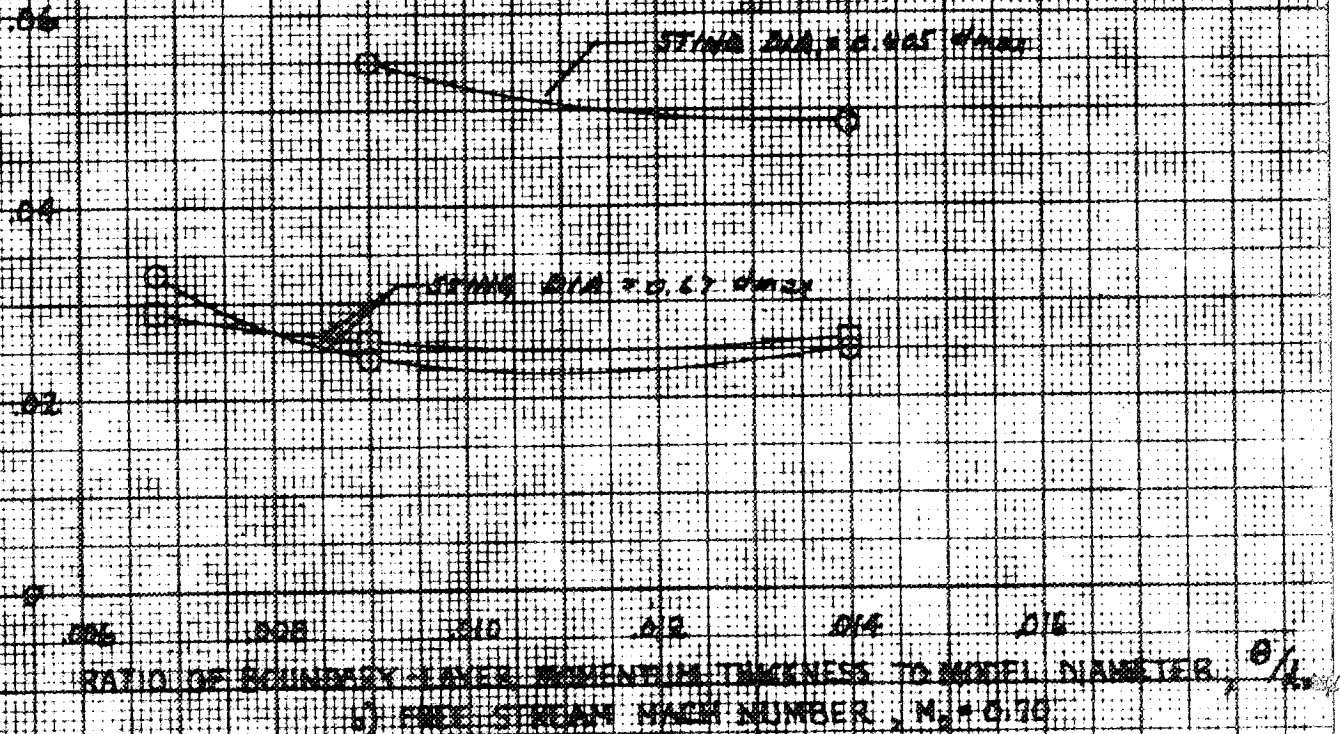
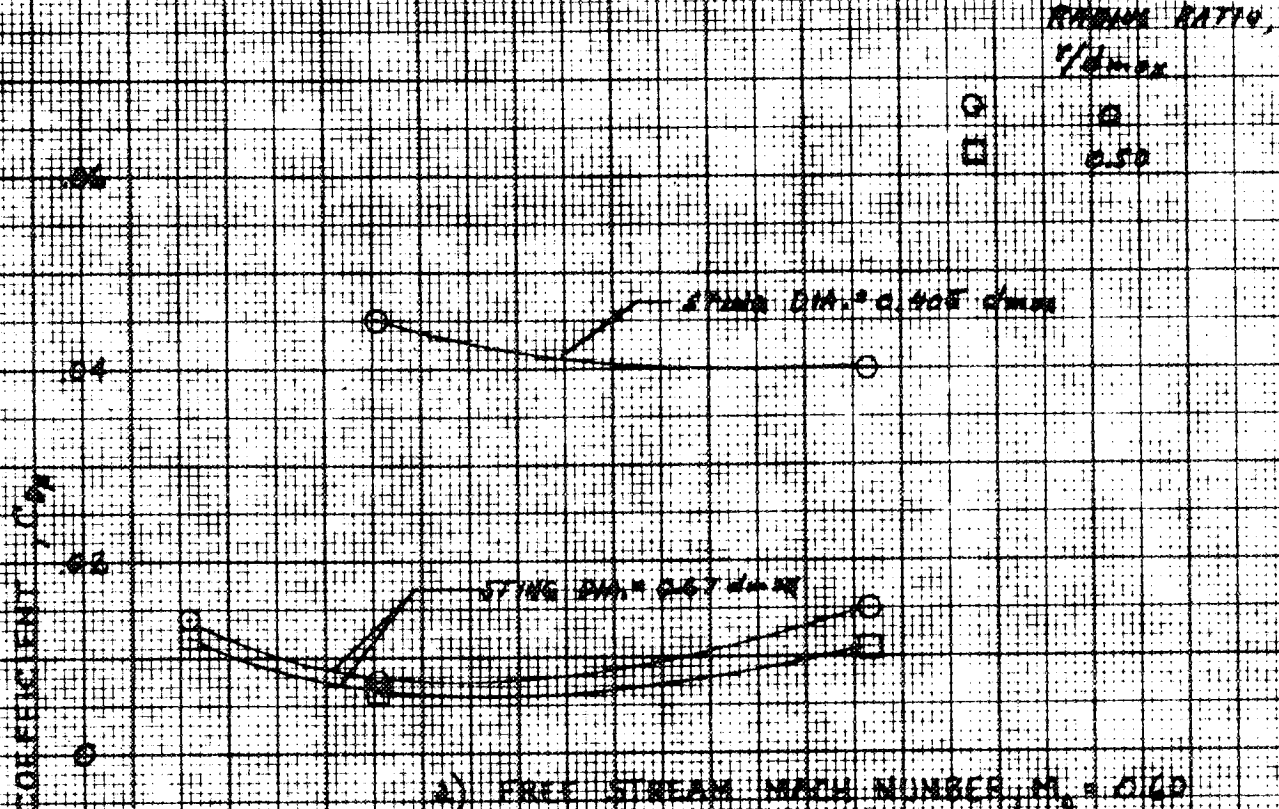
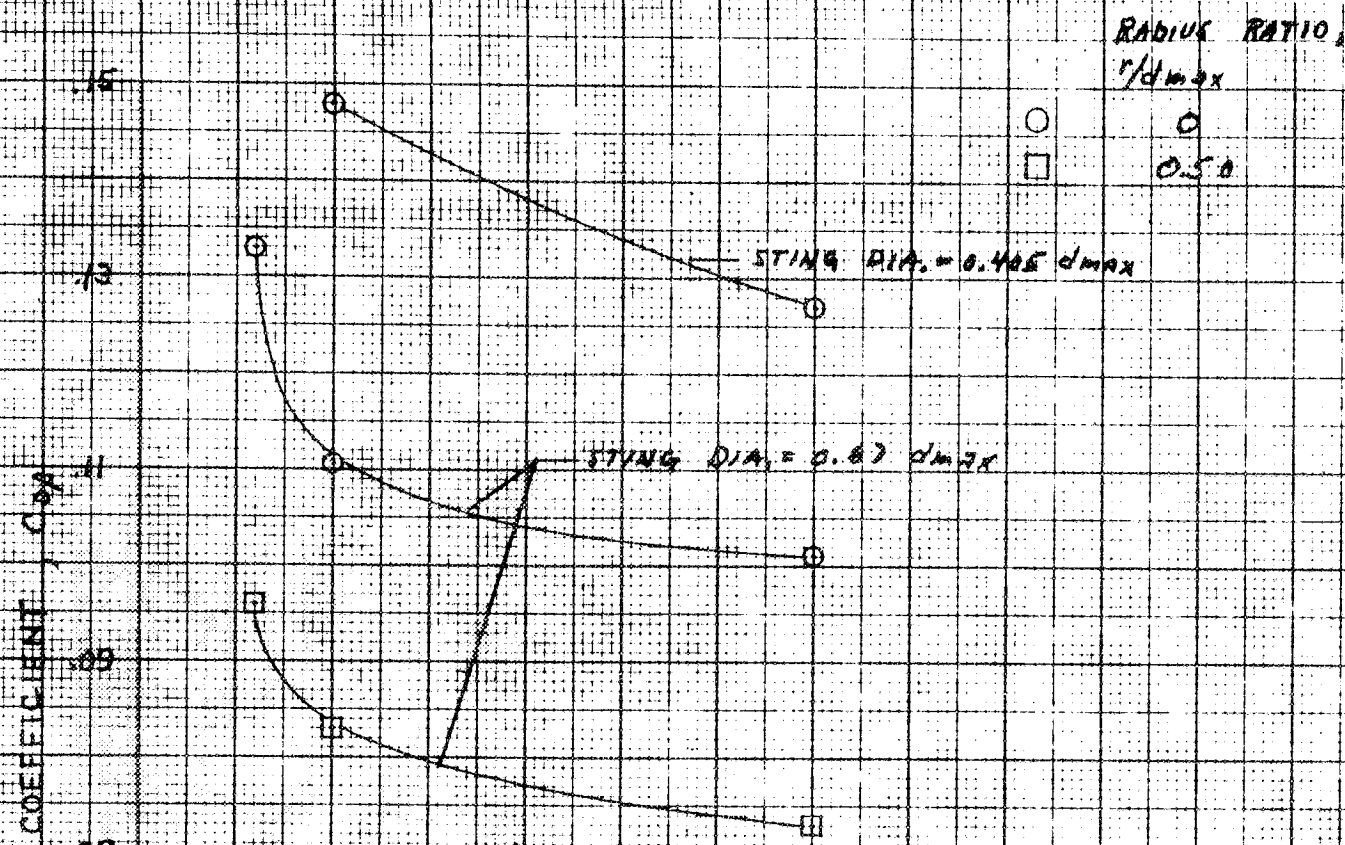


Figure 15. Effect of boundary-layer momentum thickness on boattail pressure drag; 10.16 cm model.





e) FREE STREAM MACH NUMBER,  $M_0 = 0.95$

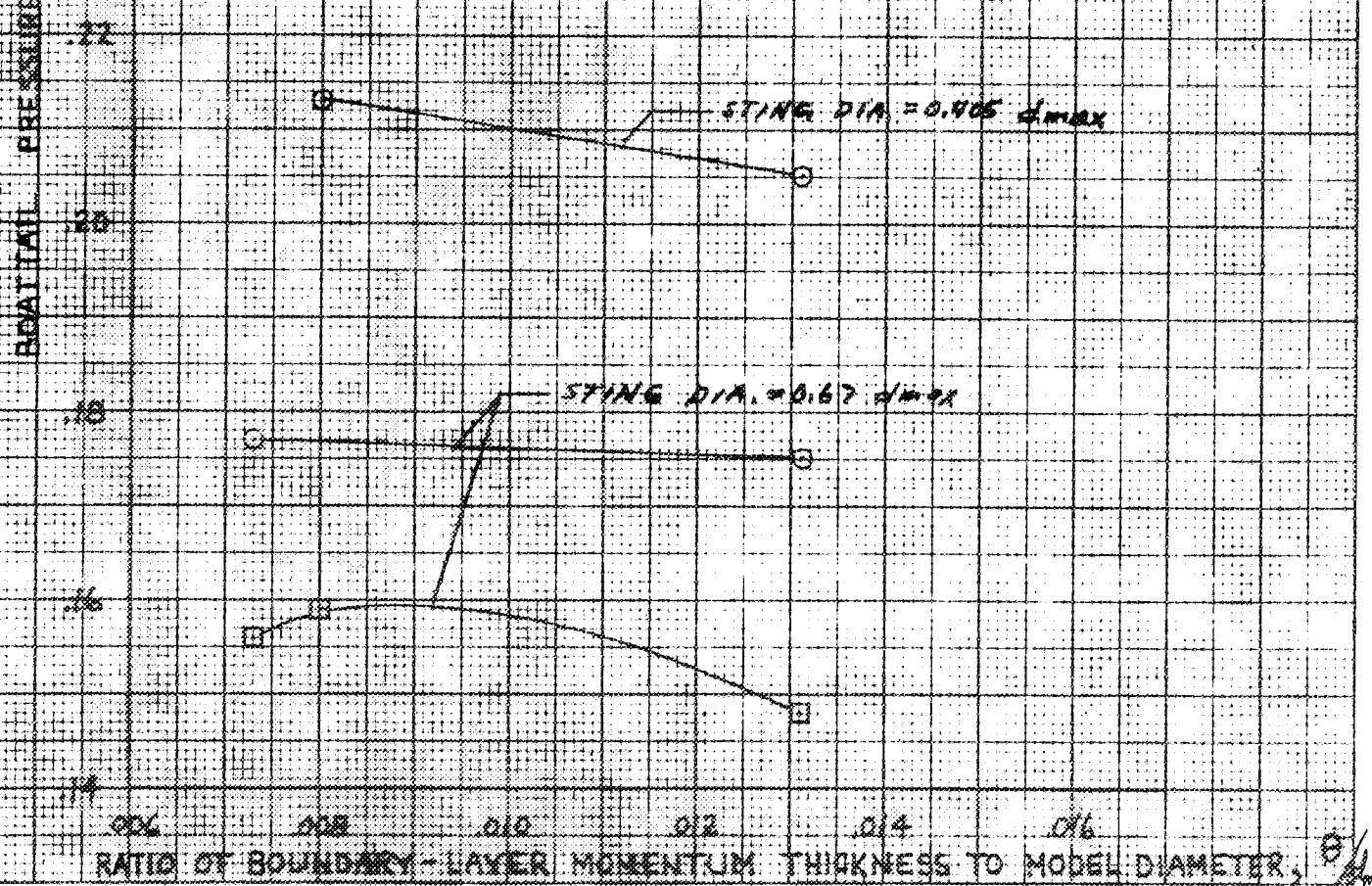


Figure 15. Concluded

○ 10.16 cm model /  
 □ 21.59 cm model /

0.24

BOTTLE DRAG COEFFICIENT,  $C_{DA}$

0.20

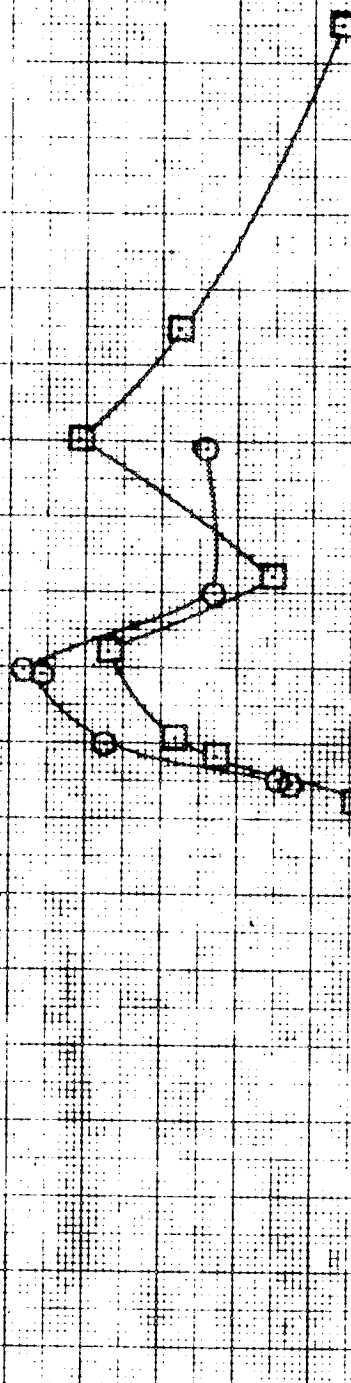
0.16

0.12

0.08

0.04

0



Free-stream Mach number,  $M_0$

Figure 16. Comparison of bottle drag coefficient measured on 21.59 cm jet-exit model to long 10.16 cm sting-supported model, 15-degree bottle,  $r/d_{max}$  zero, with jet-boundary conditions.

